Formation of residual stresses during quenching of Ti17 and Ti-6Al-4V alloys: influence of phase transformations

J. Teixeira, D. Maréchal, R.C. C Wimpory, S. Denis, F. Lefebvre, R. Frappier

Formation of residual stresses during quenching of Ti17 and Ti-6Al-4V alloys: influence of phase transformations

J. Teixeira[a,b*], D. Maréchal[a,b,1], R.C. Wimpory[c], S. Denis[a,b], F. Lefebvre[d], R. Frappier[e]

[a]UMR 7198 CNRS Université de Lorraine, Campus ARTEM, 2 allée A. Guinier, 54000 Nancy, France
[b]Laboratory of Excellence "Design of Alloy Metals for Low-mass Structures" (DAMAS), Univ. Lorraine
[c]Helmholtz-Zentrum Berlin für Materialien und Energie GmbH. Hahn-Meitner-Platz 1, 14109 Berlin, Germany
[d]CETIM Senlis, 52, avenue Félix Louat, 60300 Senlis, France
[e]Mat-In-Meca, Le Gué, 85110 Sainte-Cécile, France

*Corresponding author: julien.teixeira@univ-lorraine.fr
[1]Presenlty at: IRT-M2P, 4, rue Augustin Fresnel, F-57070 Metz, France.

Abstract
The formation of internal stresses during quenching of titanium alloys from the β phase field are investigated both experimentally and by simulation, in order to show the effects of phase transformations. Two titanium alloys are considered: the β-metastable Ti17 alloy and the α+β Ti-6Al-4V alloy. During the quench into water of laboratory scale samples (40 mm diameter cylinders), no phase transformations occurred in the Ti17 alloy because of its β-metastable character and the fast cooling. However, β→α+β and β→α' phase transformations occurred in the Ti-6Al-4V sample. Both alloys are compared in order to highlight the effects of the phase transformations. Residual stresses were determined by neutron diffraction, by the contour method and at the surface by the hole drilling method. A model for the coupled thermal, mechanical and metallurgical evolutions is established in order to simulate the quenching operations. The material model for the Ti17 alloy was established in a previous study. Regarding the Ti-6Al-4V alloy, modelling approaches and experimental data from literature are utilized to build the material model. From both experiment and simulation, it is found that the internal stress evolutions are governed by the thermal gradients. The phase transformations have a weak impact because of the small deformation strains induced by the phase change. Nevertheless, good prediction of the phase transformation kinetics is necessary for accurate simulations, because the α and α' phases strengthen the alloy, thereby limiting the plastic straining at the origin of the residual stresses. As most plastic strains are cumulated at high temperature, the thermomechanical model should be established accurately over the temperature ranges in which there is a significant proportion of β phase.

Keywords: Titanium alloys, quenching, phase transformations, residual stresses determination, simulation

1 Introduction

Microstructures and mechanical properties of titanium alloys are controlled by optimizing the sequences of thermomechanical processing. These sequences generally include several quenching operations, which give rise to the formation of residual stresses at different scales. Macroscopic or first order residual stresses, which are equilibrated at the scale of the treated parts, are of particular interest. These can reduce the fatigue life of the components, stimulate crack formations or give rise to deformations either during quenching or during machining operations. Quenching treatments also generate distortions, which can have an impact on all the next steps of the part production, until the final machining. The control of distortions is crucial in order to avoid scrap or supplementary stages to suppress these, whose economic impact may be significant [1,2]. Understanding the formation of the internal stresses is therefore necessary to optimize the treatments. This understanding goes throughout the simulation, whereas most experimental techniques only give the final microstructures and residual stresses at the end of the quenching.

In order to predict the formation of the residual stresses, one has to consider the coupled thermal, mechanical and metallurgical phenomena which occur during the quenching [3–6]. The internal stresses and the plastic deformations come in large part from the thermal gradients which are established inside the treated part during the cooling. These are enhanced in titanium alloys, which present low thermal conductivity. The phase transformations also influence the stress evolutions by modifying the local microstructure, thus the local mechanical behavior, and by inducing strains during phase change (volume change, phase transformation induced plasticity). The phase transformation kinetics is determined by the local temperature evolutions. In return, the phase transformations influence the temperature evolutions by changing the thermophysical properties and because of the latent heat released by the phase change. Finally, the internal stresses and the plastic strains can modify the phase transformation kinetics and give rise to the phase transformation induced plasticity phenomenon [7,8].

These interactions were considered for investigating the thermal treatments of steels [3,4,7–9] and aluminum alloys [10,11], making it possible to predict by simulation the final distributions of residual stresses and microstructures inside treated parts. In the case of steels, it was shown that the phase transformations have strong effects on the evolutions of internal stresses. This is due to the strains induced by the phase transformations: volume change, transformation plasticity strain. In steels, the residual stresses cannot be predicted without taking account of the effects of the phase transformations.

Titanium alloys were less studied, and the effects of the phase transformations on the internal stresses evolutions were frequently simplified or neglected (e.g. [5,12], see review in [13]). The phase transformations are really only considered in a few studies, most of these on Ti-6Al-4V and welding [14–18]. Either weak or strong effects on stress evolutions are reported. Almost all of these studies included a simulation of the coupled thermal, mechanical and metallurgical evolutions. For example, considering Ti-6Al-4V alloy welding processes in [14,15], models are introduced in detail to predict the phase transformation kinetics (on heating and cooling) and the thermomechanical behavior as a function of the multiphase microstructure, (β, α and α' phases). In [19–21], the α phase morphology was also accounted for. At high temperature (above ca. 500°C), the viscous effects have to be considered. All such studies conclude that a coupled simulation is necessary to make accurate predictions of the residual stresses; the simulation must predict the microstructure evolutions and accordingly the thermomechanical behavior of the material. This conclusion is confirmed by good agreement with experiments in [14,17].

The point of disagreement regards the consideration of the strains that are induced by the phase transformations, such as the volume change strain and the transformation plasticity strain. In [14,15], these strains are either not considered or considered negligible, which means that the only effect of the phase transformation on the stresses evolutions is to change the mechanical behavior (in [14,15], a volume change strain is introduced in the model equations, but its magnitude is not specified). In a study on fiber laser welding of Ti-6Al-4V alloy [17], it is concluded from simulations that the phase transformations have a weak impact on the residual stresses, (while the effect on distortions is more significant). This is ascribed to the small volume change strain induced by the phase transformations in titanium alloys (e.g. [22]). Conversely, in a simulation study on the selective laser melting processing of Ti-6Al-4V alloy [18], a much larger volume change strain is assumed ($\Delta V/V_0$~1%). Significant effects on the residual stresses are thus predicted.
In a simulation study on the quenching of the Ti17 alloy [16], it was found, in accordance with [17], that that the phase transformations have a limited "direct" impact because of the small volume change strain: the internal stresses evolutions during the cooling have in large part a thermal origin. Nevertheless, the accounting of the microstructure evolutions in the thermomechanical model is shown to allow more precise prediction of the residual stresses. Finally, in an experimental study on the electron beam welding of the Ti-6Al-4V alloy [23], it was observed that the distributions of residual stresses are closely correlated with the local microstructure, suggesting that the microstructure and stress evolutions were coupled. It is also proposed that the martensitic $\beta \rightarrow \alpha'$ phase transformation taking place in the fusion zone induced transformation plasticity.
These contradicting conclusions show that there is, so far, no general agreement in literature on how and to which extent the phase transformations may influence the development of first order internal stresses during the thermal processing of titanium alloys (from heat treatment, welding, etc.) The present study aims at investigating further these effects by several means. Firstly, the treatment considered here is a quenching operation. Such treatments are easier to analyze compared e.g. to the much-studied welding treatments, because the microstructure evolutions are restricted to solid state phase transformations and the thermal treatment is only cooling, without heating-cooling cycles. Also, adapted experimental methodologies are already well established [5].
Secondly, two titanium alloys will be compared: the β-metastable Ti17 alloy and the α+β Ti-6Al-4V alloy. Laboratory scale samples will be put in β phase field (solution treatment) and then quenched into water. In the Ti17 alloy, no phase transformations are expected because of the fast cooling (it will remain in full a β state). Conversely, the α+β Ti-6Al-4V alloy will undergo diffusive $\beta \rightarrow \alpha+\beta$ and martensitic $\beta \rightarrow \alpha'$ phase transformations. Comparing both alloys will highlight the effects of the phase transformations. Finally, in a simulation part, a coupled thermal, mechanical and metallurgical simulation will be established for the Ti-6Al-4V alloy, by combining models [15] and experimental data [14,19] available in literature. For the Ti17 alloy, a material model was already established [16,24].
In the following, the experimental methods are presented, as well as the results regarding the temperature evolutions during the quench, the final microstructures and the residual stresses. The latter are determined by neutron diffraction, by the contour method and by the hole drilling method. Then, a material model is introduced for the Ti-6Al-4V alloy. The material model already available for the Ti17 alloy [16] is briefly recalled. The simulation results are then presented for both alloys. Finally, the experiments and the simulations are analyzed in order to establish the consequences of the phase transformations on the formation of the residual stresses.

2 Experimental procedure and results

2.1 Studied materials

Two titanium alloys are considered: the Ti-6Al-4V alloy and the Ti17 alloy. The chemical composition of both alloys, shown in Table 1, was determined by the Titanium Metals Corporation (TIMET Savoie). The β-transus of both alloys was determined by resistivity measurement.

Alloy	Al	Cr	Mo	V	Sn	Zr	O	T_β (°C)
Ti17	5.1	4.0	4.1	-	2.0	2.0	0.11	880
Ti-6Al-4V	6.6	-	-	4.1	-	-	0.20	1010

Table 1. Alloy compositions in wt. %, β transus.

The mill-annealed as-received microstructure of the Ti-6Al-4V alloy contains α and β phases, with less than 10% β phase. The initial microstructure of the Ti17 alloy is also α+β, with an α phase amount of approximately 70%. The β grain size was measured after a solution treatment in β domain followed by isothermal transformation in a dilatometer in order to "decorate" the β grain boundaries with α phase. The average β grain size is 600 µm in both Ti17 and Ti-6Al-4V alloys. The initial microstructures result from a thermomechanical treatment which led to preferred orientations in the billet. The presence of this crystallographic texture did not affect the phase transformation kinetics, but may affect the dimensional behavior resulting from quenching.

2.2 Quenching experiments

2.2.1 Experimental conditions

The quenching experiments were carried out in a furnace (NAGAT E20/40P), which includes a heating chamber, a quenching tank and a transfer chamber linking both parts. The transfer of the sample from the heating chamber to the quenching tank was achieved automatically, which ensured good reproducibility and transfer duration below 5 s. The treatments were realized under reducing atmosphere of nitrogen and 5% hydrogen with slight over-pressurization. The contamination by the hydrogen was confined to the edge of the samples and less than 75 ppm, according to chemical analyses. The quenching was performed in salt water (15 g/L of salt) to avoid film boiling which may induce non reproducible cooling (e.g. [25]). The water was continuously stirred and its temperature ranged between 30°C and 40°C during quenching.

The selected sample geometry consisted of cylinders with 40 mm diameter and 100 mm length for both alloys. According to preliminary simulations, this diameter was sufficient to allow significant residual stresses. The length was large enough to consider an infinitely long cylinder (no effect of longitudinal temperature gradients on the median plane). Three samples were heat-treated for each alloy. In the first sample, four thermocouples were located in the median plane according to the schematic in Figure 1. They were positioned at the center of the cylinder and at 9 mm, 13.3 mm and 16.5 mm from the center. This first sample also served for microstructure and hardness characterizations, in the median plane. Both other samples, instrumented with one single thermocouple located at 20 mm under the top surface, were dedicated to residual stress determinations, either by neutron diffraction or by destructive methods (hole drilling, contour). Each thermocouple was crimped with threaded stainless steel tubes to prevent penetration of water into the holes. The thermocouples were K-type, 1.5 mm in diameter, with Inconel sleeve.

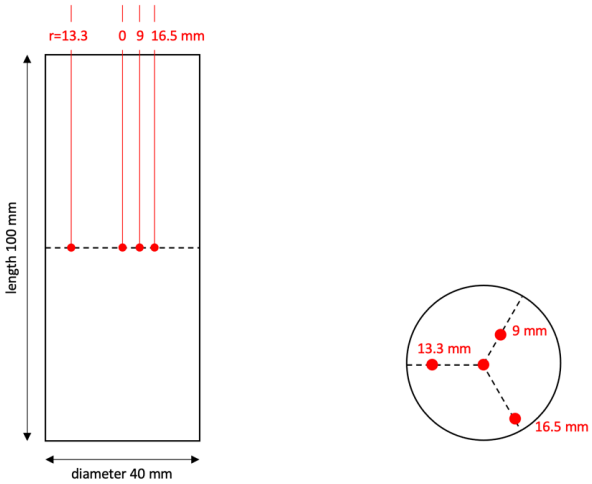

Figure 1. Instrumentation of the cylindrical samples with thermocouples.

The samples were solution-treated in the β phase and quenched into water. The heating chamber was pre-heated at the β solution treatment temperature (T_{ST}), 920°C for Ti17 alloy and 1070°C for Ti-6Al-4V alloy, before introducing the sample. The time necessary to reach T_{ST} in the core was 15 min. The samples were left for an additional 15 min at T_{ST}, for a total stay of 30 min in the heating chamber, before quenching. It was verified with experiments in a dilatometer that full α dissolution was achieved with this thermal treatment, and that β grain growth was limited. The average β grain size reached 750 µm for the Ti17 and 600 µm for the Ti-6Al-4V.

2.2.2 Ti17 alloy

The temperature evolutions measured in the median plane during the quenching of the Ti17 sample is presented in Figure 2 (black dots). The cooling rates were too fast to allow any phase transformation. Even at the center, the cooling rate was largely higher than the critical rate (1-2°C.s^{-1} above 400°C, where phase transformation kinetics are significant [24]). No exothermic effect of any phase transformations was observed and the absence of phase transformation was confirmed by microstructural observations and by X-Ray diffraction. Consequently, the full cylinder remained in the β phase. The same observation was reported previously for a similar experiment [24]. The maximum temperature difference reached 380°C between the center and the thermocouple closest to the surface. This large difference is likely to produce significant residual stresses. The comparisons with numerical simulations will be discussed later on.

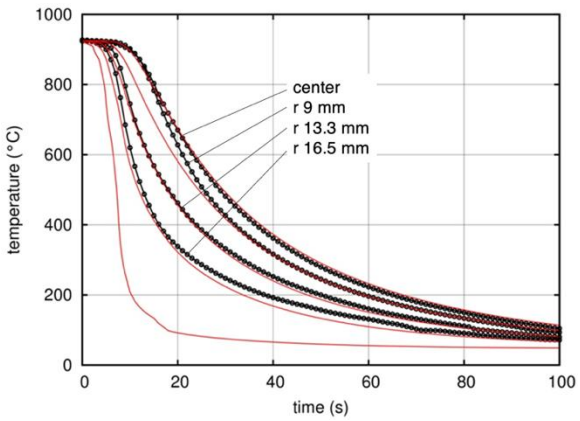

Figure 2. Temperature evolutions during quenching of Ti17 sample at four thermocouple positions (see Figure 1) and at the surface, measured (black dots) and calculated (red lines) according to the model presented in section 3.1. Simulation at the surface is also plotted.

2.2.3 Ti-6Al-4V alloy

The temperature evolutions measured in the median plane of the Ti-6Al-4V sample during quenching is presented in Figure 3 (black dots). The exothermic effect of the β→α phase transformation is clearly visible around 840°C, especially in the center. The curve of the thermocouple closest to the surface crossed that of the nearest thermocouple below. This can be ascribed to a possible displacement of the thermocouple in the hole during the movements of the cylinder during the transfer from the furnace to the quenching tank. The temperature difference between the center and the thermocouple closest to the surface reached 450°C (this is higher than for Ti17), so that significant residual stresses can be expected too. Calculated results (temperature evolutions and transformation kinetics) are also plotted and will be analyzed in Section 4.

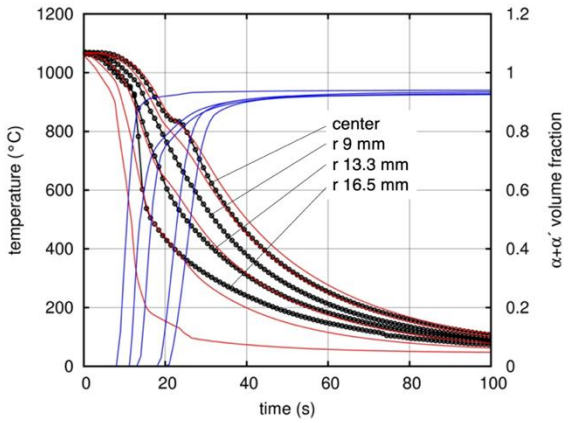

Figure 3. Temperature evolutions during quenching of Ti-6Al-4V sample at four thermocouple positions (see Figure 1) and at the surface, measured (black dots) and calculated (red lines). Simulation at surface is also plotted. In blue: α+α' volume fraction versus time according to simulation, at each radius considered.

The temperature gradients which appeared during the quenching experiment generated microstructural gradients. Microhardness measurements were carried out in a slice of cylinder, cut out at the median plane. Vickers microhardness measurements (with 500 g load) were done every 0.5 mm along three radii of the slice. These measurements are presented in Figure 4. A gradient of hardness is clearly demonstrated, increasing from ca. 310 HV in the center to 400 HV at the surface. The hardness curve shows a plateau between the center and a radius of 7.5 mm. These values are in agreement with those reported in literature for similar cooling rates [26,27]. Faster cooling rates near the surface led to higher hardness. This is ascribed to finer microstructures and higher proportion of α' martensite. From X-ray diffraction performed in the laboratory (with Cu and Co sources), it was possible to detect only the α phase. From synchrotron X-ray diffraction (in transmission, at DESY P07 line), a few peaks of β phase could be detected. Statistics was not sufficient, however, to determine the β phase mass fraction. Nevertheless, these experiments confirmed that, at the end of quenching, there remained a low amount of β phase (less than 10%).

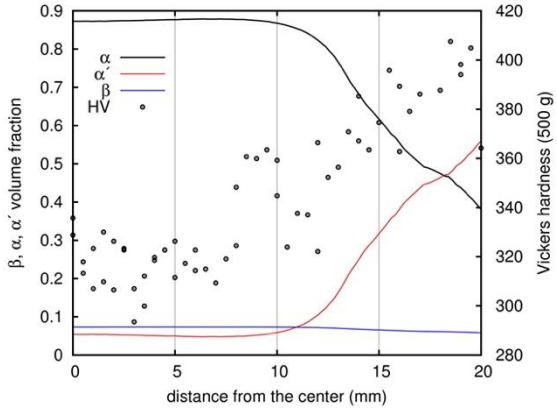

Figure 4. Measured hardness radial profiles in the median plane of Ti-6Al-4V sample and simulated α, α' and β phase amounts profiles, at the end of the quenching. (Center and edge of the cylinder at 0 mm and 20 mm respectively).

Optical micrographs of the microstructure are presented in Figure 5. There is no clear difference between the center and the surface. In both microstructures, at least three morphologies are present: (i) thin continuous layers along the prior β grains boundaries, (ii) colonies of nearly parallel lamellae emanating from the grain boundaries and (iii) intragranular. Both first intergranular morphologies correspond to the α phase [28]. The intragranular morphology may consist of both α and α' phases. According to [29], the α' martensite is composed of long, thin and orthogonally oriented plates. The intragranular α phase has a more tangled "basketweave" microstructure. Finer microstructure characterization was not carried out here, because in the present study the influence of the α phase morphology on the mechanical behavior was not considered (see Section 3.3).

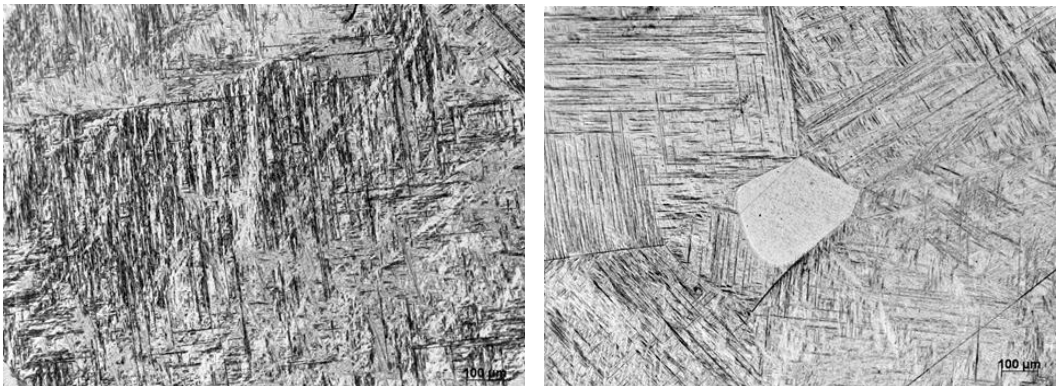

Figure 5. Optical micrographs of the microstructure in the Ti-6Al-4V alloy sample after quenching. a) at the center; b) near the surface (note that the small grain in bright contrast is filled with α/α' phase lamellae).

2.3 Residual stresses determinations

2.3.1 Neutron diffraction

Neutron diffraction experiments were carried out on the E3 diffractometer at the Helmholtz Zentrum (HZB) in Berlin, Germany. A neutron wavelength of 1.47 Å was obtained with a Si (400) monochromator. The neutron flux was ca. 5.10^6 $cm^{-2}.s^{-1}$. Data acquisition was realized with the Caress software, which was developed at HZB. The results were then processed with StressTexCalculator software (v. 1.53 [30]).

Acquisitions were realized in the median plane of the cylinders along one radial direction at positions spaced out from 2 mm, from the surface to the center, plus an additional point at

radius 19 mm (1 mm under the surface). The inter-reticular distances were measured in radial, hoop and axial directions. For each direction, the sample was positioned appropriately (Figure 6). Due to the large grain size, the sample was rotated around a vertical axis (referred to as ω angle) in order to sample a larger volume. Radial and hoop acquisitions consisted of 11 scans, while axial acquisition consists of 17 scans with a rotation of ω=1° between each scan.
Figure 6 schematizes the beam trajectory and the diffracting gage volume, which consists of a prism with a nearly rhombus base, whose largest dimension is about 5 mm. The height of the prism is 9 mm for Ti17 alloy and 19 mm for Ti-6Al-4V alloy. It was increased for the latter to improve the statistics. For each position along the radius, the acquisition time was 60 min for radial and hoop directions, including all the ω scans. For the axial direction, the acquisition lasted between 100 and 180 min, because the counting time was increased at higher depth (i.e. r < 10 mm). After acquisition, the 11 or 17 scans were summed up with StressTexCalculator in order to obtain well-contrasted portions of Debye-Scherrer rings.
Four examples of images collected by the detector are presented in Figure 7. The images were integrated in order to obtain a I(2θ) diagram, as shown in Figure 7.
The $\{211\}_{\beta}$ reflection was utilized for the Ti17 alloy, which was in a full β state. The second low-intensity peak at 2θ~1° apart from the 1st peak is a well-known artifact from the monochromator. A better contrast was obtained in radial than in hoop direction, due to the different sample lengths crossed by the neutron beam.
Only the $\{11\bar{2}2\}_{\alpha}$ reflection was used for the Ti-6Al-4V alloy:

- The $\{10\bar{1}3\}_{\alpha}$ reflection could be altered by small amount of β phase.
- The $\{20\bar{2}1\}_{\alpha}$ reflection could be altered by the monochromator artifact from the $\{11\bar{2}2\}_{\alpha}$ reflection.
- The $\{20\bar{2}0\}_{\alpha}$ and $\{0004\}_{\alpha}$ reflections were too weak to be utilized.

The β phase could not be studied in the Ti-6Al-4V alloy due the too low amount of this phase.

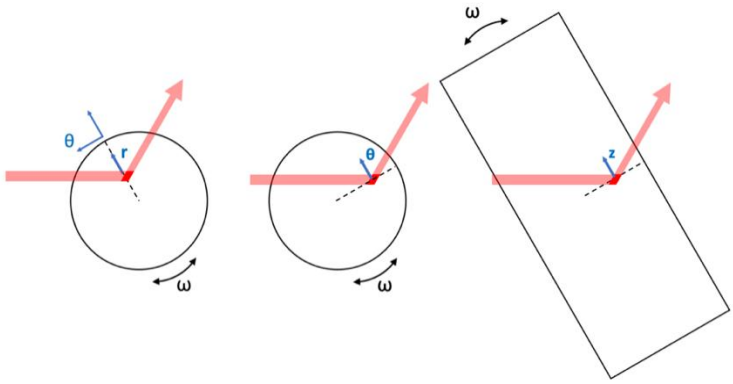

Figure 6. Schematic of the beam trajectory and sample layout to determine the strain in radial, hoop and axial directions. Approximate shape of the diffracting volume is represented in red.

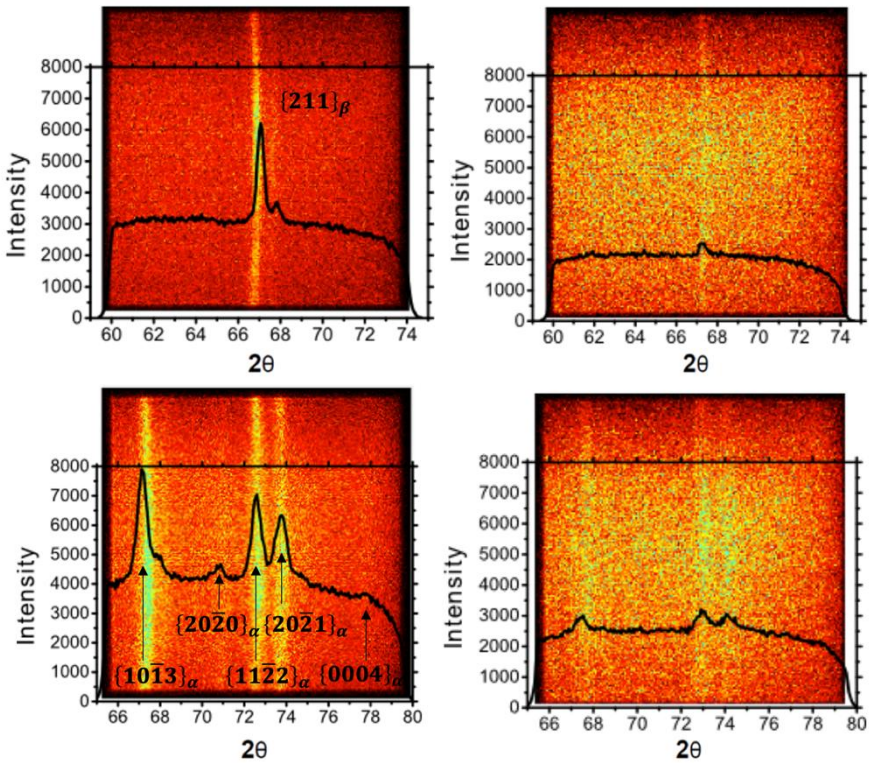

Figure 7. Images collected by the detector (integration of the ω scans) and I(2θ) diagrams in Ti17 sample (top) and Ti-6Al-4V sample (bottom), along radial (left) and hoop (right) directions, taken at radius 19 mm (1 mm under the surface of the cylinder).

The StressTexCalculator software allows to represent the considered diffraction peaks with a Gaussian function after background subtraction. The 2θ angles associated with the selected peaks were then determined with a precision[1] between ca. 0.005° and 0.035°, depending mostly on the length of the beam trajectory inside the sample. The inter-reticular distance could then be deduced from Bragg's law, $d_{hkl} = \lambda/(2\sin\theta)$. In order to calculate the strain, the inter-reticular distance free of macroscopic stress, noted d^0_{hkl}, must be known. For the Ti17 alloy, d^0_{hkl} for β phase was obtained from a dilatometric specimen, a cylinder with 14 mm length and 4 mm diameter taken from the same billet as for the more massive cylinder. It underwent the same thermal treatment as near the surface of the massive cylinder and it is assumed that thermal gradients are very small and do not generate macrostresses. For the Ti-6Al-4V alloy, in the massive cylinder, the microstructure gradient could *a priori* be associated with a gradient of d^0_{hkl}. Thus, to determine d^0_{hkl} a methodology described for instance in [32] was followed. Another massive cylinder was quenched in similar conditions. From this cylinder, a comb-like specimen was cut out by electro discharge machining (EDM) in the mid-plane along the diameter. The 9 teeth of the comb were 10 mm long and 2.2 mm wide. They were oriented along the axis of the cylinder. In this method, it is assumed that the cautious machining relieved the stresses so that the macroscopic stress is equal to zero inside the comb teeth. (But there could be lower-order stresses). Both Ti17 and Ti-6Al-4V reference

[1] The uncertainty in 2θ, $u(2\theta)$, is estimated from fitting the data with a Gaussian function using the least squares method. The value obtained is approximately that of the formula [31] $u(2\theta)^2 \cong \left(\frac{SD^2}{I}\right)\left[1 + 2\left(2^{\frac{1}{2}}\right)\frac{B}{H}\right]$, where SD is the standard deviation of the Gaussian function (FWHM=2(2ln2)$^{1/2}$ * SD), I the integrated intensity (this should be the number of neutrons in the Gaussian peak, after taking account of the data binning). B/H is the background to Gaussian peak height ratio. This uncertainty is then propagated when computing the strains and stresses.

d^0_{hkl} samples were analyzed with the E3 diffractometer. Despite the observed microstructural gradient, it was actually found that d^0_{hkl} for the alpha phase did not vary significantly along the diameter in Ti-6Al-4V.

Knowing the inter-reticular distance in the massive specimen and in the reference, the strain was calculated according to:

$$\varepsilon_i = \frac{\sin\theta^0_{hkl}}{\sin\theta^i_{hkl}} - 1 = \frac{d^i_{hkl} - d^0_{hkl}}{d^0_{hkl}} \quad (1)$$

where *i*=*r*,θ or *z* denotes the radial, hoop or axial direction, d^i_{hkl} and $d^0_{hkl}$are the inter-reticular distance in the massive and reference specimens, measured along direction *i* in the massive sample and in one single direction in the reference sample. The stress was calculated from Hooke's law:

$$\sigma_i = \frac{E_{hkl}}{1+\nu_{hkl}}\left[\varepsilon_i + \frac{\nu_{hkl}}{1-2\nu_{hkl}}(\varepsilon_r + \varepsilon_\theta + \varepsilon_z)\right] \quad (2)$$

where E_{hkl} and ν_{hkl} are the radio-crystallographic elastic constants of the considered {hkl} plane. For the α phase, values tabulated for pure titanium [33] were employed $E_{11\bar{2}2}$= 113 GPa, $\upsilon_{11\bar{2}2}$=0.32. For the β phase an Eshelby-Kröner model developed at HZB was employed: E_{211}= 99 GPa, ν_{211}= 0.33.

2.3.2 Hole drilling method

The hole drilling method is one of the stress relief methods. These methods consist in analysing the stress relief which occurs in a component when material removal is carried out by machining. The distortion measurements generated by such stress relief makes it possible, through analysis of the successive equilibrium states, to go back to the values of the residual stresses that existed in the part before material removal. In this study, the purpose of the hole-drilling method was to provide the macro residual stresses and more accurate measurements near the surface in terms of spatial resolution. The incremental hole-drilling method was carried out at CETIM, Senlis, France, to determine the residual stresses near the surface. Unidirectional TML-FRS-2-11 gages were stuck on the median plane. Displacements were monitored by an MGC+ measuring station. Hole drilling was carried out with a universal milling machine with 5 mm diameter one-piece carbide tungsten milling cutter. Drilling depth was 2.5 mm in order to respect the boundary condition and the standard ASTM E837 [34]. The measuring station directly computed the stresses using Hooke's law with the following elastic constants: E=99.3GPa, ν=0.333 for Ti17 [35,36]; E=110.5GPa, ν=0.317 for Ti-6Al-4V [19].

2.3.3 Contour method

The contour method provides a 2-dimensional map of residual stresses over a cross-section of a component using a single cut. Unlike diffraction techniques, the contour method is not sensitive to microstructural variations and has been successfully applied to various components [37–43]. Furthermore, the contour method is not limited by the geometry and thickness of the tested components and has been applied to large and complex geometries [40,44]. The contour method is a destructive method which evaluates residual stresses by the evaluation of strains due to cutting. It is based on the superposition principle and is divided into three steps: cut the specimen using wire electro-discharge machining (EDM), measure

the out of plane deformation profile of both cut surfaces, process both experimental profiles to finally perform an inverse stress analysis in a finite element (FE) simulation. The stress calculated on the cut surface is a true representation of the residual stress component normal to the plane of cut that was present in the sampled volume.
The cutting was performed in the median plane of the cylinder with a Fanuc Robocut A-C600iB with a brass wire after wrapping and clamping. Prior to the cut, sacrificial parts were fabricated. The sacrificial part had typically a square section with a round clearance adjusted to the round shape of the cylinder. The aim of the sacrificial part is to keep constant the apparent thickness to be cut (electrical parameters and speed are kept constant to get constant material surface parameters) and to mitigate cutting artefacts. The profilometry was carried out with Alicona infinite focus machine with optimized filtering for data interpolation (algorithms under Python). Spatial resolution of the probe was about 25 µm.
For calculating the displacement profile, several data processing steps are followed (Mat-In-Meca's proprietary algorithm). Alignment of the data sets for opposing cut surfaces is corrected. Then a basic filter is applied to delete measurement artefacts and error points, and to reduce potential excessive roughness. Each data set is interpolated by a numerical 2D spline function, which is then discretized for the modeling. Then, both discretized data sets are averaged to remove errors due to shear stress and anti-symmetric EDM travel errors.
To calculate the stresses in an FE model, the geometries of the cut parts were created and meshed with tetrahedral elements in Gmsh 4.4.1 software [45]. FE simulations were prepared and performed with the Aster code [46]. The model was assigned uniform isotropic elastic properties, the same as for the hole-drilling method (Section 2.3.2).
Uncertainty on the data processing is evaluated based on the approach described in [47]. Standard errors between 1 MPa and 23 MPa are estimated in the present results. Nevertheless, other sources of uncertainty exist (cutting, sample locations, etc.). Standard uncertainty ±50 MPa is thus considered in the present study.

2.3.4 Results

The elastic strains determined in the Ti17 alloy sample by neutron diffraction (ND) are shown in Figure 8a. The most reliable component was the radial strain, the less reliable was the hoop (tangential) strain, due to the longer sample length crossed by the beam. For axial and radial components, the uncertainty was lower near the surface. For the hoop strain, the uncertainty was high even near the surface due to the trajectory of the beam. Evidently, the errors on the strains have an impact on all the calculated residual stress components, radial, hoop and axial.
Figure 8b shows the profiles of residual stresses in the Ti17 sample. From neutron diffraction, it comes out that these profiles are characteristic of purely thermally induced stresses. The axial stress was compressive at the surface (~ -300 MPa) and tensile in the center (~ +200MPa). As expected from the cylindrical geometry, hoop and radial stresses were nearly equal at the center, while radial stress tended to zero when approaching the surface. The hole drilling method also gave compressive stresses at a depth 2.5 mm from the surface. The discrepancies between ND and hole drilling will be discussed beneath. This figure also shows simulated results that will be discussed later on.

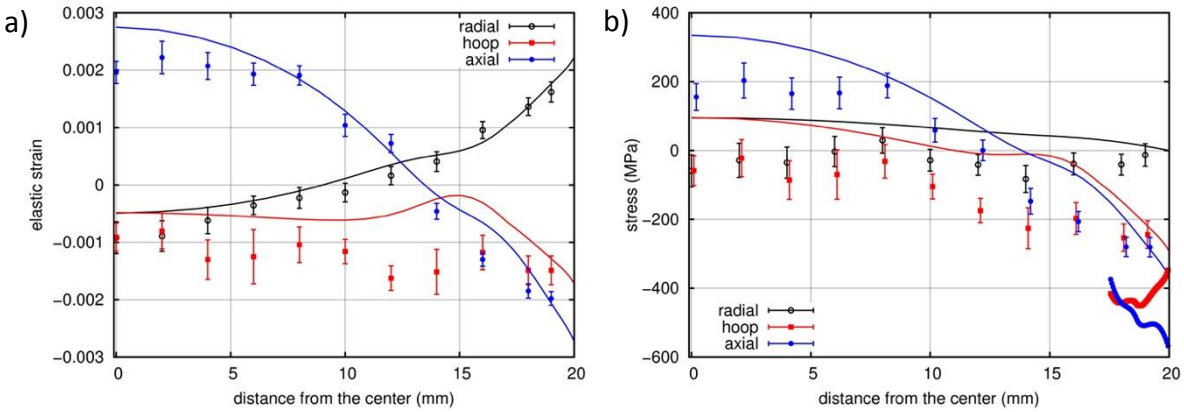

Figure 8. a) Elastic strain and b) residual stress radial profiles in Ti17 sample median plane, determined experimentally from neutron diffraction (dots) and hole drilling method (bold lines in b). Calculated stress profiles (thin lines) by numerical simulations. (Center and edge of the cylinder at 0 mm and 20 mm respectively).

Figure 9a shows the elastic strain radial profile in the Ti-6Al-4V sample. The same observations as for the Ti17 sample can be made regarding the uncertainties. Thanks to the increased acquisition time, the uncertainties were lower than those in Ti17. The grain size was smaller in the Ti-6Al-4V alloy, because a large number of α grains are formed inside the β grains (but with 12 crystallographic variants per β grain in maximum). Figure 9b shows the experimental residual stress profiles in the Ti-6Al-4V sample. These profiles are similar to the non-transforming Ti17 sample, showing that the phase transformations did not modify dramatically the overall aspect of the profiles. The axial stress was compressive at the surface (~ -400 MPa) and tensile in the center (~ +600 MPa). However, the stress levels were significantly higher than those in the Ti17 sample. Regarding the hole drilling method, the same observation as for Ti17 alloy can be made: higher axial stress in comparison with neutron diffraction and a large decrease of the hoop stress towards the surface.

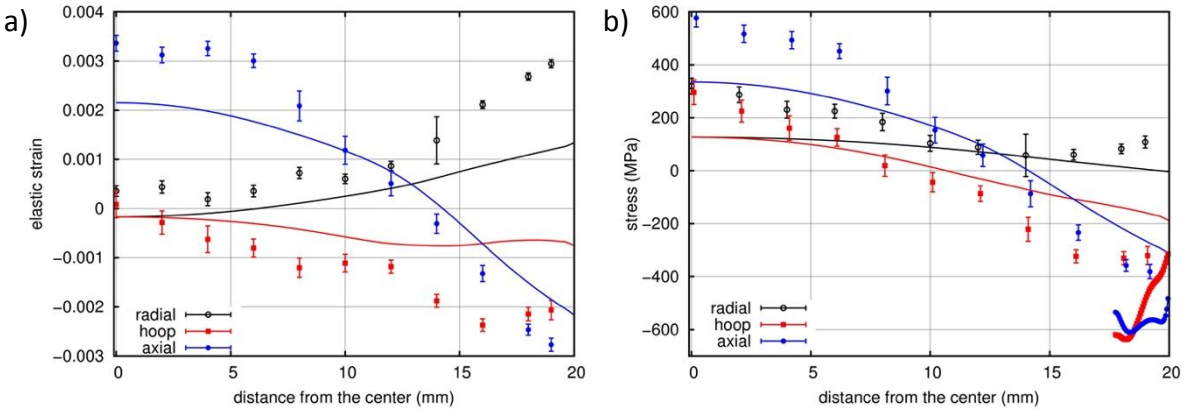

Figure 9. a) Elastic strain and b) residual stress radial profiles in Ti-6Al-4V sample median plane, determined experimentally from neutron diffraction (dots) and hole drilling method (bold lines in fig b). Calculated stress profiles (thin lines) obtained by numerical simulations. The latter show the average of stresses calculated in α and α' phases. (Center and edge of the cylinder at 0 mm and 20 mm respectively).

Figure 10a shows the axial residual stress map in the median plane of the Ti-6Al-4V cylinder, according to the contour method. In agreement with the results from neutron diffraction, it

shows tensile residual stresses in the center and compressive residual stresses near the surface. The stresses distribution is not perfectly cylindrical. A possible origin is that during the cooling, the heat flux extracted from the cylinder surface was not uniform. Radial profiles along four different directions were extracted from the 2D map, and are plotted in Figure 10b. Except for the profile D, these profiles are close to each other and the most significant spread occurs near the surface. Similar results were obtained for the Ti17 alloy.

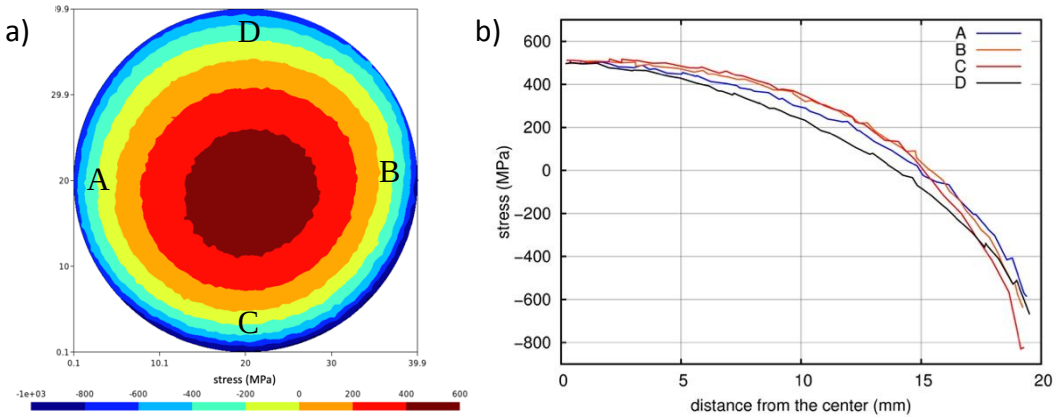

Figure 10. a) Two-dimensional map of the axial residual stresses determined by the contour method in the median plane of the Ti-6Al-4V cylinder. b) Axial stress radial profiles along four different directions labeled in Figure a).

Figure 11 compares axial stresses profiles determined by neutron diffraction, contour method and hole drilling. For the Ti-6Al-4V, (Figure 11b), a very good agreement is obtained between the neutron diffraction and the contour method. Near the surface, the last point from ND (at 19 mm) has to be considered with care, as the diffraction volume went partly outside the cylinder. The contour and hole drilling methods are in good agreement at 19 mm. The contour method becomes less reliable closer to the surface. Conversely, the hole drilling becomes less precise deeper in the cylinder. The same comments can be done regarding the Ti17 alloy (Figure 11a). The contour method confirms that the residual stresses are lower in Ti17 than in Ti-6Al-4V, as shown by the neutron diffraction. However, there is a significant discrepancy in the center of the cylinder between the ND and the contour method, which give a residual stress of ca. 200 MPa and 300 MPa respectively. There is no clear origin for this difference.

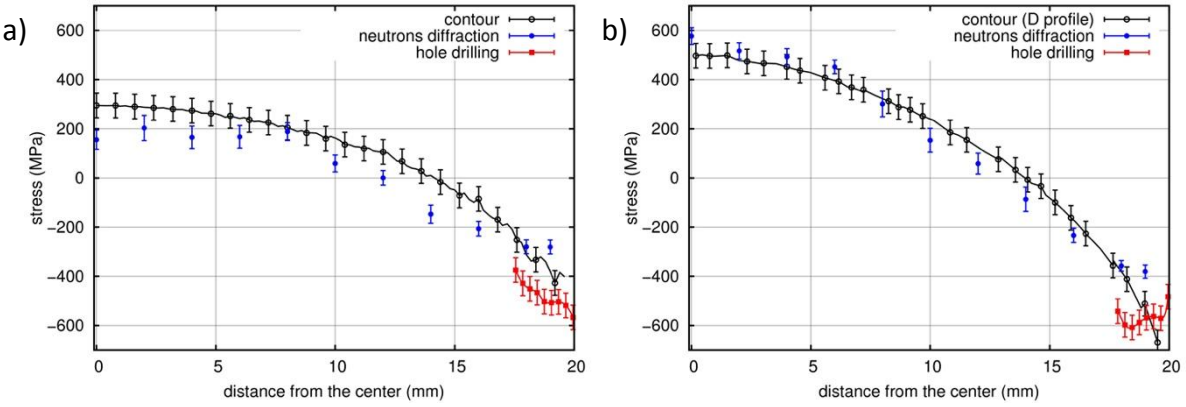

Figure 11. Comparison between the axial residual stress profiles determined by the contour method, by neutron diffraction and by hole drilling. a) Ti17; b) Ti-6Al-4V. (Center and edge of the cylinder at 0 mm and 20 mm respectively).

3 Material Model

The material model utilized for the Ti17 alloy was presented in previous studies [16,24]. As the Ti17 sample remained in the β phase during quenching, a coupled thermal and mechanical simulation was carried out, considering the thermal and mechanical behavior of the β phase only. The thermal and mechanical models and associated data were presented respectively in references [24] and [16]. For the Ti-6Al-4V alloy which exhibited the β→α transformation during quenching, a coupled thermal, new metallurgical and mechanical model is required.

3.1 Thermal calculation

The temperature distribution within a part during a thermal treatment is calculated by solving numerically the heat conduction equation by the using the Finite Element method (see Section 3.4):

$$div(\lambda gradT) + \dot{q} = \rho C_P \frac{\partial T}{\partial t} \tag{3}$$

where T is the temperature, λ the thermal conductivity, C_P the specific heat, ρ the density, t the time and the source term $\dot{q}$ is the rate of heat generation due to the phase transformation (in our case the exothermic β→α+β or β→α' phase transformations in Ti-6A-4V alloys).

$$\dot{q} = \Delta H \frac{dz}{dt} \tag{4}$$

where ΔH is the enthalpy of transformation per unit volume and dz/dt is the rate of transformation (in our case z is the α+α' phases volume fraction). The thermophysical parameters λ, ρ and C_P depend on the temperature and the microstructure, as will be seen in Section 3.3.3 on model parameters.

The boundary condition at the surface is:

$$-\lambda \frac{\partial T}{\partial n}\Big|_S = \Phi = h(T_S - T_\infty) \tag{5}$$

where Φ is the surface heat flux density, h the heat transfer coefficient, T_S the temperature at the surface and T_∞ the temperature of the quenching medium. $\partial T/\partial n|_S$ is the temperature gradient normal to the surface

3.2 Metallurgical model

For the Ti17 alloy, it was seen that no phase transformation occurred during the quench into water, because the cooling rate was too fast and because this alloy is β-metastable. (A model to predict the phase transformation kinetics in this alloy is nevertheless presented in [24]).

For the Ti-6Al-4V alloy, the phase transformation kinetics are sufficiently fast to occur. Two morphologies of α phase forming with diffusional mechanism were established in previous studies. Inter- and intra-granular morphologies form respectively at high and low transformation temperature range [28]. Nevertheless, in the present model, no difference is made and the α phase is considered as one single phase transformation product. As presented

in Section 2.2.3, the respective amounts of the different α phase morphologies could not be quantified experimentally.

Martensite (α') can be formed in the Ti-6Al-4V alloy with a displacive mechanism, according to some studies. It has a hexagonal compact structure [48], like the α phase. α and α' phases are difficult to discriminate by X-ray diffraction due to close cell parameters. Nevertheless, Malinov et al. achieved this by considering the Full width at half maximum (FWHM) [49]. According to Ahmed and Rack [29], the critical cooling rate necessary to form martensite is 410°C.s^{-1}. In [14,15,50], martensite was observed despite slower cooling rates. There are also discrepancies in the literature regarding the reported Ms temperatures, which span a large range, from 575 to 800°C .

In the present model, the Kolmogorov-Johnson-Mehl-Avrami (KJMA) approach is employed to describe the diffusive β→α+β phase transformation kinetics. Isothermal kinetics are described with the KJMA rule and an additivity hypothesis is made to predict the kinetics on cooling. Isothermal kinetics are essentially described with the equation:

$$z^{\alpha} = z^{\alpha}_{max}[1 - exp(-k(t - t_S)^n)] \tag{6}$$

where z^{α} is the volume fraction of α phase, z^{α}_{max} the maximum fraction of α phase, which depends on temperature, t_S the incubation time. k and n are the KJMA kinetic parameters. The parameters z^{α}_{max}, t_S, n and k are tabulated as a function of temperature on the basis of experimental data. In the simulations, this relationship is differentiated to calculate the kinetics as a function of time (see [24]).
Variations of z^{α}_{max} in Ti-6Al-4V alloy with temperature were established in many studies, leading to significant discrepancies. The same formula as in [14] is employed:

$$z^{\alpha}_{max}(T) = 0.925\left[1 - exp\left(-0.0125(980 - T)\right)\right] \tag{7}$$

where the temperature is in degrees Celsius. (Actual transus is 1010°C for the studied material (Table 1), but this has a weak impact on the simulations).

The kinetic parameters t_S, n and k have to be established from experimental kinetics of isothermal transformation. Isothermal transformation (IT) diagrams of the Ti-6Al-4V alloy were established in several studies [28,50,55]. But, as the phase transformation kinetics highly depends on variations of alloy composition or initial β grain size, we established some isothermal kinetics for our own alloy. Three isothermal treatment temperatures were applied: 750, 850 and 950°C after β solution treatment for 15 min at 1070°C. Our set of KJMA kinetics parameters were deduced by combining our kinetics data and the data from literature.
The displacive β→α' transformation is described with the Koistinen-Marburger equation. It is assumed that it starts at the Ms temperature. The diffusive β→α+β phase transformation then ceases. The volume fraction of α phase remains then constant during subsequent cooling. The fraction of α' martensite is then calculated as follows:

$$z^{\alpha'} = (1 - z^{\alpha})\left[1 - exp\left(-\alpha_{KM}(M_S - T)\right)\right] \tag{8}$$

The M_S and α_{KM} parameters are set at 650°C and 0.005 K^{-1} on the basis of literature data. z^{α} is the fraction of phase formed until Ms.

3.3 Thermomechanical model

3.3.1 Multiphase model for the Ti-6Al-4V alloy

The mechanical model for the Ti-6Al-4V alloy allows to predict an estimate of the average stresses and strains specific to each phase β, α and α' and a satisfactory description of the macroscopic behavior. It also takes account of the effect of β→α+β or β→α' phase transformations. In this study, we utilized the model of [14,15], which was introduced for the modeling of laser assisted processing of Ti-6Al-4V alloy, which involves microstructural and mechanical evolutions similar to present study on cooling. This model is summarized here.
Each phase (ϕ=β, α, α') affords a local stress tensor. A "β rule" [56,57] gives the scale transition between the macroscopic scale and the scale of the phase. The local stress is the sum of the macroscopic stress and an accommodation term:

$$\underline{\sigma_\phi} = \underline{\sigma} + \mu\left(\underline{\beta} - \underline{\beta_\phi}\right) \text{ with } \underline{\beta} = \sum_\phi z_\phi \underline{\beta_\phi} \tag{9}$$

Where $\underline{\sigma_\phi}$ is the stress in phase ϕ, $\underline{\sigma}$ is the macroscopic stress, μ is the shear modulus, z_ϕ is the volume fraction of phase ϕ, $\underline{\beta_\phi}$ is an accommodation variable specific to each phase. The accommodation term is thus proportional to the difference between $\underline{\beta_\phi}$ and the average of the $\underline{\beta_\phi}$variables among the different phases. The evolution law of $\underline{\beta_\phi}$ reads for each phase:

$$\dot{\underline{\beta}}_\phi = \dot{\underline{\varepsilon}}_\phi^{vp} - D_\phi \underline{\beta_\phi} \dot{p}_\phi \tag{10}$$

Where $\underline{\varepsilon}_\phi^{vp}$ is the viscoplastic strain in phase ϕ, D_ϕ is a parameter characterizing the scale transition and p_ϕ is the cumulated equivalent plastic strain in phase ϕ.
The dynamic recovery term of previous equation is negligible, because of the small plastic deformations which occur during quenching treatments. It will be seen in the results (Section 4) that the plastic strains will remain below 0.5%, according to the simulations. As shown by equation 10, the $\underline{\beta_\phi}$ variables reduce to $\underline{\varepsilon}_\phi^{vp}$ when the plastic strain is small. Therefore, it was assumed that $D_\alpha = D_\beta = 0$. One can mention that in [14,15], the dynamic recovery term was more important, because this study considered larger strains associated with laser assisted processing (such as welding), which induces several successive thermal cycles. In contrast, in present study, only one cycle occurs (e.g. tension followed by compression near the surface). It was found that either using the D_α and D_β values identified in [14] (respectively 150 and 170) or assuming that D_α and $D_\beta = 0$ did not have significant impact on our simulations.
An elastoviscoplastic behavior is assumed for each phase. The total macroscopic strain is decomposed into the following components under the small deformation hypothesis: indeed, it is well known that quenching treatments lead to small deformations of the order of one percent (see e.g. [7]):

$$\dot{\underline{\varepsilon}} = \dot{\underline{\varepsilon}}^e + \dot{\underline{\varepsilon}}^{vp} + \dot{\underline{\varepsilon}}^{th} + \dot{\underline{\varepsilon}}^{tr} + \dot{\underline{\varepsilon}}^{tp} \tag{11}$$

where $\dot{\underline{\varepsilon}}^e$ is the elastic strain rate, $\dot{\underline{\varepsilon}}^{vp}$ is the viscoplastic strain rate, $\dot{\underline{\varepsilon}}^{th}$ is the thermal strain rate, $\dot{\underline{\varepsilon}}^{tr}$ is the strain rate associated with volume change induced by the phase transformation. $\dot{\underline{\varepsilon}}^{tp}$ is the phase transformation induced plasticity strain rate.

Homogeneous and isotropic elasticity is assumed ($\underline{\sigma}$ and $\underline{\varepsilon}^e$ are related to each other with Hooke's law, all phases have the same Young's modulus and Poisson coefficient). Isotropic thermal expansion coefficient is assumed. All the phases are assumed to have the same thermal expansion coefficient for simplicity. Hence,

$$\underline{\varepsilon}^{th} = \alpha(T_0 - T)\underline{I} \tag{12}$$

where α is the thermal expansion coefficient assumed to be constant, T_0 the temperature at the beginning of the quenching, T the temperature and $\underline{I}$ the identity tensor (isotropic thermal expansion is assumed).

The phase change strain is due to the volume change associated with the phase transformation. Isotropic phase transformation strain is assumed.

$$\underline{\varepsilon}^{tr} = \delta\left(z^{\alpha} + z^{\alpha'}\right)\underline{I} \tag{13}$$

where δ is one third of the relative volume variation associated with a complete transformation from β to α or α'. It is assumed to be the same for both β→α and β→α' phase transformations. Impact of this key parameter is discussed in 5.2.2.
The viscoplastic behavior of each phase is described by assuming a Von Mises yield criterion. The yield function reads for each phase ϕ:

$$f_\phi = J\left(\underline{\sigma}_\phi\right) - R_{0\phi} - R_\phi\left(p_\phi\right) \tag{14}$$

where $J\left(\underline{\sigma}_\phi\right)$ is the second Von Mises invariant of stress tensor $\underline{\sigma}_\phi$, $R_{0\phi}$ is the yield stress and the function R_ϕ describes the isotropic work-hardening as a function of the cumulated equivalent plastic strain p_ϕ:

$$R_\phi\left(p_\phi\right) = Q_\phi\left[1 - exp\left(-b_\phi p_\phi\right)\right] \tag{15}$$

where Q_ϕ and b_ϕ are parameters which depend on the temperature.

A Norton power law is utilized to calculate the rate of increase of the cumulated equivalent plastic strain:

$$\dot{p}_\phi = \left(\frac{f_\phi}{K_\phi}\right)^{n_\phi} \tag{16}$$

where K_ϕ and n_ϕ are parameters which depend on the temperature.

The viscoplastic strain rate is calculated as:

$$\underline{\dot{\varepsilon}}_\phi^{vp} = \underline{n}_\phi \dot{p}_\phi \tag{17}$$

where $\underline{n}_\phi$ is the normal to the yield surface (n=∂f/∂σ).

$$\underline{n_\phi} = \frac{3}{2}\frac{\underline{s_\phi}}{J(\underline{\sigma_\phi})} \quad (18)$$

where $\underline{s_\phi}$ is the deviator of $\underline{\sigma_\phi}$. Contrary to [14,15], we assume isotropic hardening and no recovery during phase transformation.

A final feature of the model is the full inheritance by the α or α' phases of the plastic deformation in the β phase, when the phase transformations occur.

3.3.2 Single β phase model for Ti17 alloy

The thermomechanical model for the Ti17 alloy was presented in [16]. For the Ti17 alloy, no phase transformation has to be considered as shown in Section 2.2.2. Hence, the mechanical simulations for the Ti17 alloy will be carried out by considering that the alloy remains in single β phase state. The main assumptions of the mechanical model are the same as for the Ti-6Al-4V alloy: isotropic elasticity and thermal expansion, Von Mises yield criterion, isotropic hardening. Viscous effects are accounted for with a modified Norton law representing the dynamic yielding phenomenon occurring with β phase [58]. The equations are detailed in reference [16].

3.3.3 Model parameters

3.3.3.1 Thermoelastic and thermophysical behavior

The Young's modulus and the Poisson's coefficient of the β phase in the Ti17 alloy were taken from [35,36]. In the Ti-6Al-4V alloy for which homogeneous elasticity is assumed (Section 3.3.1), the values of E and ν are taken from [19]. These parameters depend on the temperature in both alloys.

The thermophysical properties of the different phases are taken from [59] for the Ti17 alloy and from [14] for the Ti-6Al-4V alloy. They depend on the temperature and the microstructure (a mixture rule on α and β volume fractions is applied on C_P, ρ and λ). The enthalpy of the β→α+β phase transformation in Ti-6Al-4V alloy was determined by differential scanning calorimetry and is equal to 2.4 10^8 $J.m^{-3}$. The evolution of heat transfer coefficient versus surface temperature was obtained through an "inverse method" (adjustments based on the temperature measurements). Upon quenching in vaporizable fluids, complex phenomena govern the heat transfer from the cylinder surface to the quenching medium. This regards especially the instability of the boiling film, which makes these phenomena unreproducible, and makes very difficult to establish a physics-based calculation of the heat transfer coefficient (see e.g. [3]).

3.3.3.2 Thermal strain

The thermal expansion coefficient of the β phase in Ti17 alloy is deduced from in situ synchrotron X-ray diffraction measurements [60] of the β phase lattice parameter during the cooling of Ti17 samples from the β phase field: α^β = 13.5 10^{-6} K^{-1}. As for the Ti-6Al-4V alloy, one single thermal expansion coefficient is used for both α and β phases, on the basis of our dilatometry experiments: $\alpha^\alpha = \alpha^\beta$ = 10 10^{-6} K^{-1}.

3.3.3.3 Phase transformation strain

The phase transformation strain is assumed to be equal to zero on the basis of our dilatometry experiments. Accordingly, in literature, no significant or very small strain associated with the β→α+β or β→α' phase transformations is reported in Ti-6Al-4V alloy [22]. The consequence of this assumption on the simulations will be discussed in Section 5.2.2.

3.3.3.4 Phase transformation plasticity strain

The transformation plasticity strain increment is determined, as in previous works, according to the following relationship [16]:

$$d\underline{\varepsilon}^{tp} = \frac{3}{2}\frac{d\varepsilon^{tp}}{\overline{\sigma}}\underline{s} \tag{19}$$

where $\underline{s}$ is the deviator of the total stress tensor $\underline{\sigma}$ and $\overline{\sigma}$ is the corresponding Von Mises equivalent stress. $d\varepsilon^{tp}$ represents the equivalent transformation plasticity strain increment:

$$d\varepsilon^{tp} = K^{tp}\overline{\sigma}(dz + dz') \tag{20}$$

The constant K_{tp} is estimated as [61]:

$$K^{tp} = \frac{5}{6}\frac{1}{\sigma_e}\frac{\Delta V}{V_0} \tag{21}$$

where σ_e is the yield strength of the softer phase, the β phase. It is estimated from the equation 22 (see the next Section), taking account of the work-hardening (parameter d in equation 22 is taken equal to p_β the cumulated equivalent plastic strain).

These relationships were derived from the of Greenwood-Johnson model [4,61], which concerns the plastic strains originating from the accommodation of the transformation strain.

3.3.3.5 Thermo-visco-plastic behavior

The parameters of the mechanical model for the β phase in the Ti17 alloy were identified in [16] on the basis of the experimental study of [62] and will be used here. The methodology and the assumptions are detailed in [16].

For the Ti-6Al-4V alloy, the mechanical model parameters must be determined for three phases: β, α and α'. The parameters for the β phase are taken from [14], using a basis of specific experiments and the literature [63,64]. It is assumed that the martensite (α') and the α phase have the same behavior; this will be justified in the simulations. The mechanical model parameters for the α/α' phase were identified on the basis of the thermomechanical characterizations carried out in the study of R. Julien et al. [19], which also focused on quenching treatments. In the present work, we selected one part of these experiments as a basis to establish the model parameters. In these experiments, the tensile samples were solution treated at 950°C for 2h, in the α+β phase field, then cooled at 60°C.min^{-1} down to the considered temperature, which was kept constant during the tensile test. The total strain was 1% and different strain rates 10^{-4}, 10^{-3} and 10^{-2} s^{-1} were applied in order to determine the viscoplastic behavior.

From the experimental curves for α+β mixtures, we have determined by an inverse method the behavior of the individual α phase by considering the behavior of the β phase taken from [14]. Some recalculated tensile curves for α+β mixtures are compared with the experimental ones in Figure 12 for the temperature range 700-950°C, which is the one of interest for the simulations, as will be seen later. There is a good agreement between the simulation and the experiment, showing that the effects of the temperature and the strain rate are well captured. The detailed shape of the stress-strain curves is well described at 900°C and 700°C, showing the ability of the model to predict the tensile behavior of the α+β mixture. At 950°C the flow stress is also correctly predicted, but there are some discrepancies at low strains, which come from the fact that the dynamic yielding (the drop of the flow stress at the beginning of the tensile test) is not accounted for. Detailed accounting of the dynamic yielding such as in

[24,58] was not carried out here. The reason is that, in the Ti-6Al-4V alloy, this phenomenon is significant at strain rates higher (~10^{-2} s^{-1} and larger) than those encountered in present study. For the Ti17 alloy, the dynamic yielding phenomenon is more significant and it was thus accounted for in detail in [24].

Figure 13 shows the 0.2% conventional proof stress of the α+β mixture between 20 and 1000°C. For each phase, it is estimated as:

$$\sigma_{0.2\%}^{\phi} = R_0^{\phi} + R^{\phi}(d) + \sigma_{visc}^{\phi} \tag{22}$$

where d=0.002 and σ^{ϕ}_{visc} is the viscous stress, estimated as:

$$\sigma_{visc}^{\phi} = K^{\phi}\dot{\varepsilon}^{\frac{1}{n^{\phi}}} \tag{23}$$

It is assumed that the α phase fraction follows the equation 7. Three strain rates 10^{-4} s^{-1}, 10^{-3} s^{-1} and 10^{-2} s^{-1} are considered and experimental values from [19] are shown for comparison. It can be seen that the viscous effects are significant above 400°C, in accordance with [14,15]. Linear variation of $\sigma_{0.2\%}^{\phi}$ is assumed between 20°C and 300°C, on the basis of previous studies (on Ti-6Al-4V and other titanium alloys) [14,15,65].

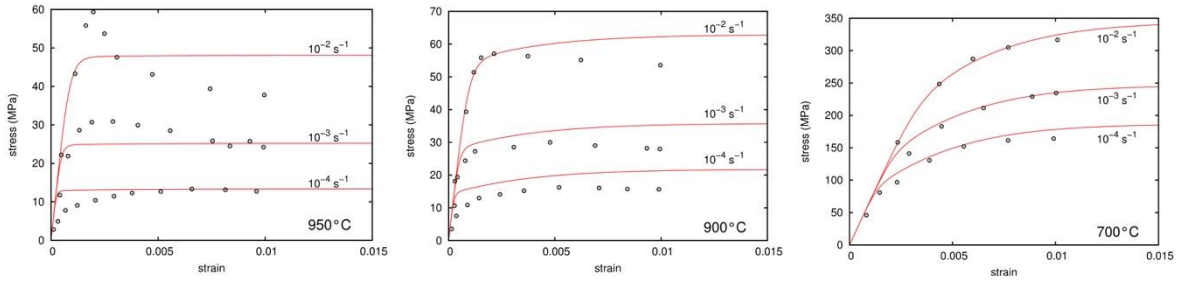

Figure 12. Stress-strain curves at different strain rates and temperatures, experimental (dots) [19] and simulated (continuous lines), for the Ti-6Al-4V alloy. 950°C, 900°C and 700°C: α+β mixtures with 43%, 66% and 90% of alpha phase respectively.

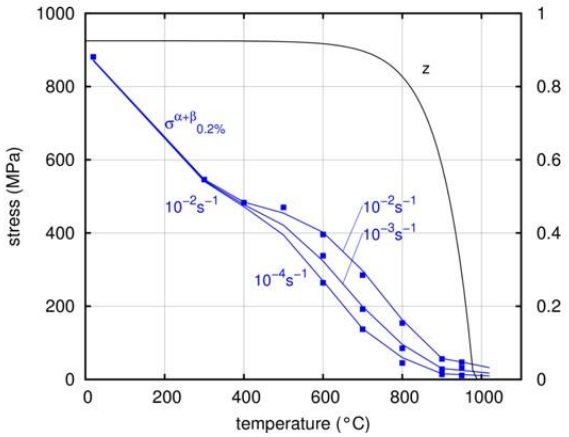

Figure 13. Simulated $\sigma_{0.2\%}$ of the α+β mixture in Ti-6Al-4V alloy assuming $z=z_{max}$ and strain rates 10^{-4} s^{-1}, 10^{-3} s^{-1} and 10^{-2} s^{-1} (blue lines) dots: experimental values from [19].

3.4 Numerical implementation

The coupled simulation of the temperature, mechanical evolutions and phase transformations kinetics was implemented in the Finite Element (FE) code Zébulon [66]. At each time step, the temperature field and the stress and strain evolutions are calculated with the FE method, whereas the phase transformation kinetics is computed as a function of the local temperature. The three simulations are inter-dependent, as all the model parameters depend on the temperature and the microstructural state. The phase transformations also induce the heat source term (Section 3.3.3.3) and the strains associated with volume change or phase transformation plasticity (Section 3.3.3.4). The latter strain depends on the local macroscopic stress. The thermal calculation is already implemented in the Zébulon code, whereas the metallurgical and mechanical calculations were implemented in our study by using the ZebFront interface. The cylinders were represented by an axisymmetric 2D rectangular domain with eight-nodes quadratic elements.

4 Simulations

4.1 Without phase transformations: Ti17 alloy

4.1.1 Temperature evolutions

Figure 2 shows the comparison between the temperature calculated and measured at the four points of measurement. There is globally a good agreement between the simulation and the experiment as expected since an inverse method has been used for the determination of heat transfer coefficient. As mentioned in Section 2.2.2, there is no phase transformation inside the Ti17 alloy cylinder, due to the too fast cooling. Hence the alloy remains in single β phase during the cooling. The thermophysical parameters of the β phase were extrapolated below the transus temperature [24], which can also lead to discrepancies for this particular simulation, in the interior of the cylinder. The temperature calculated at the surface is plotted in addition. According to the simulation, the temperature difference between the surface and the center goes up to 697°C.

4.1.2 Stress-strain evolutions and distributions

Figure 14 shows the evolution of the axial stress at the surface and the center of the cylinder during the quench into water. These evolutions are typical of thermally induced (see e.g. [67]): in a first stage, until ca. 10 s, the surface is put in tension and the center in compression, because the surface cools faster than the center. These internal stresses overcome the yield strength and viscoplastic strains are cumulated during this stage, as will be shown below. The surface of the cylinder is thus plastically extended, whereas the center is plastically compressed. As will be seen hereafter, after 10 s, no more significant plastic strains will occur. This is due to a decrease of the stresses, as the center then cools faster than the surface, thereby reducing the temperature gradients. There is then an inversion of the stresses and at the end of the cooling, there are no more temperature gradients and residual stresses remain. These residual stresses are due to the plastic deformations which were cumulated at high temperature. At the end of the quench (beyond the represented time scale), the surface has a compressive residual stress (-367 MPa) and the center a tensile stress (335 MPa).

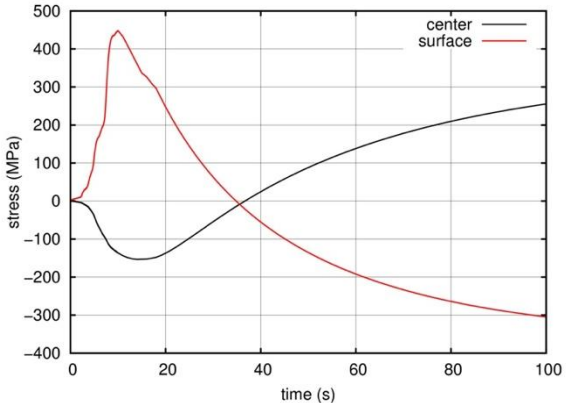

Figure 14. Evolution of the axial stress at the surface and the center according to the simulation.

Figure 15a shows the evolution of the cumulated equivalent plastic strain (p^{β}) in the β phase (the only phase present in the Ti17 alloy) as a function of the temperature in the center and at the surface. At the surface, the plastic strain increases up to 0.41% over a large temperature range, from 920°C down to ca. 350°C. In the center, the plastic strain increase stops at 800°C, because the stresses are lower in this point (Figure 14). Nevertheless, the plastic strain reaches 0.34%, which is close to the surface value, because the cylinder remains at high temperature

for a longer time in the center. The radial profiles of p^{β} plotted at different times (Figure 15b) show that the plastic straining stops sooner near the surface than near the center, as expected from the faster cooling. There is a minimum of plastic strain at radius 15.5 mm. This region of the cylinder undergoes a fast cooling and low internal stresses, which leads to smaller plastic strains.
The comparison between simulated residual stress profiles and measurement by neutron diffraction (Figure 8b) show rather a good agreement near the surface. In the center, the calculated residual axial stress is largely overestimated, but it is in better agreement with the determinations from the contour method (Figure 11a). It can be noticed that in the radius area 12-16 mm radial and hoop compressive residual stresses are underestimated by the simulation.

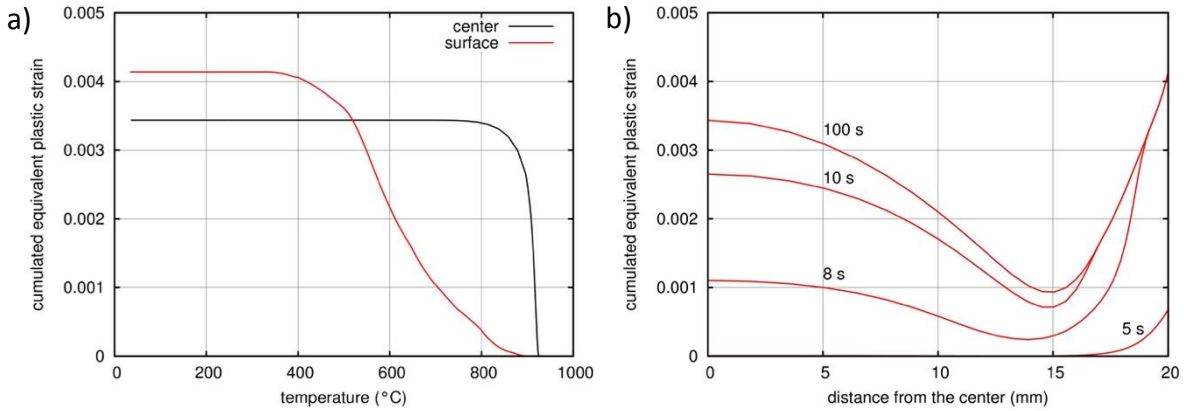

Figure 15. Cumulated equivalent plastic strain in β phase: a) in the center and at the surface as a function of the temperature; b) radial profiles in the median plane at different times.

4.2 With phase transformations: Ti-6Al-4V alloy

4.2.1 Coupled temperature and microstructure evolutions

Figure 3 shows the comparison between the measured and calculated temperature evolutions at the four points of measurement. The curve calculated at the surface is also plotted to highlight the large temperature gradients near the surface. The temperature difference between the surface and the center goes up to 780°C according to the simulation. The simulations are in good agreement with the experiment at both thermocouples closest to the surface (radii 13.3 and 16.5 mm). For the latter, one is reminded that the inverse determination of the h parameter imposed the simulation to be close to the experiment. The simulations are also in satisfactory agreement with the measurement at radius 9 mm and at the center, where the slowdown of cooling due to the phase transformation (heat release) is well predicted. Nevertheless, the temperature is sometimes overestimated by up to 100°C. This can be ascribed to the thermophysical properties of the β phase, which were extrapolated under the transus temperature. This may have an impact on the calculations until the start of the phase transformations. Then, the phase transformations make more difficult to estimate the heat transfer coefficient.
The simulated phase transformation kinetics are also plotted in Figure 3. The curves show the sum of the α and α' phases volume fractions. At each point, the latent heat released by the phase transformation induces a slowdown of the cooling. As expected, the phase transformation is shifted to longer times in the interior of the cylinder because of the slower cooling. Phase transformation kinetics in the center and at the surface are plotted vs. temperature in Figure 16. The phase transformation occurs in higher and narrower

temperature range in the center than at the surface. In the center, the β→α+β phase transformation starts at ca. 850°C and is nearly complete at 650°C. Then, few martensite (ca. 5%) forms from the Ms temperature (650°C) down to the room temperature. At the surface, the β→α+β phase transformation starts at ca. 850°C; the fraction of α reaches 37% at 650°C Then, 56% of martensite forms from 650°C to the room temperature. Hence, the different temperature evolutions at each point of the cylinder lead to microstructure gradients, with more martensite near the surface because of the high cooling rate, whereas the center has more α phase.

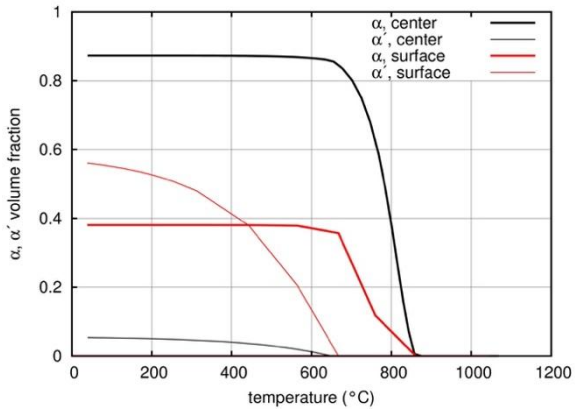

Figure 16. Evolution of α+α' phases volume fraction as a function of the temperature in the center and at the surface according to the simulation.

Figure 4 shows the radial profiles of α, α' and β phase fractions predicted by the simulation at the end of the quench. Two regions of the cylinder can be distinguished: an inner part at radii below 10 mm inside which the phase fractions are nearly constant, and an outer part where the fraction of α' phase increases from 5% at 10 mm to 56% when approaching to the surface. Correspondingly, the volume fraction of α phase is the lowest at the surface (38%) and it increases up to 87% at radius 10 mm. The volume fraction of β phase is nearly constant and less than 10% throughout the entire radius. These simulations are in good agreement with the hardness measurements: the hardness is nearly constant inside an inner radius of 10 mm; it increases from 310 HV at 10 mm to 400 HV at the surface. The higher hardness near the surface comes both from the higher fraction of martensite and from finer morphology of the α phase.

4.2.2 Stress-strain evolutions and distributions

The temperature gradients induced internal stresses during the quench. Figure 17 shows the evolution of the axial stress at the center and the surface according to the simulation, along with the phase transformation kinetics. The evolutions are typical of stresses induced by a quench operation, as detailed for the case of the quench of the Ti17 alloy (Section 4.1.2). The surface, which cools faster, is first put into tension up to 400 MPa at about 15 s, whereas the center is put into compression, with stresses of lower magnitude (maximum 115 MPa). As the temperature difference between the center and the surface is decreased, a stress reversal occurs after 15 s: the tensile stress at the surface and the compressive stress in the center decrease and later on the surface goes into compression and the center into tension. At the end of the quench (beyond the represented time scale), predicted residual stresses are -260 MPa at the surface and +260 MPa at the center.

The phase transformations affected temporarily the evolutions of the stresses, but these remained governed by the temperature gradients in the cylinder. Such temporary effects of the phase transformations were interpreted in more detail in similar simulations on Ti17 alloy [16]. These effects come from the change of mechanical behavior, from the heat released by the phase change. When the phase transformation occurs at some point of the cylinder this affects the whole distributions of the stresses. Nevertheless, their evolutions remain typical of thermal-induced stresses.

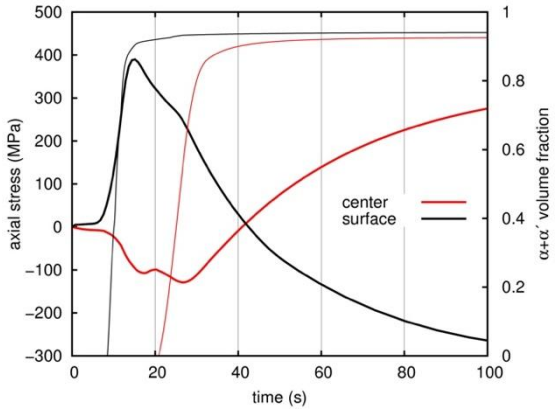

Figure 17. Evolution of the axial stress at the surface and the center according to the simulation; thin lines: phase transformation kinetics (α+α' volume fraction).

The internal stresses induced plastic deformations during the quench. Figure 18 shows the cumulated equivalent plastic strain as a function of temperature in β, α and α' phases, at the center and the surface of the cylinder. Both at the surface and the center, the most significant part the plastic straining occurred in α and β phases in a high temperature range, above ca. 750°C. Below this temperature, internal stresses are too low and/or the alloy has too high yield stress to undergo plastic straining. All the plastic straining in the cylinder occurred during the first 30 seconds of the quench. The highest plastic strains occurred in the center, where p^{β} and p^{α} reach 0.44% and 0.26% respectively. The plastic strain was higher in the center than at the surface, because the temperature remained higher for a longer time, thereby increasing the viscoplastic strains. The plastic strains are lower in α than in β phase because the α phase had less time to deform after its formation and because of its higher yield strength. The martensite did not undergo significant plastic strain, because of its low temperature of formation, below 650°C. This justifies the simplification made in the thermomechanical model, where the same mechanical behavior was assumed for α and α' phases (Section 3.3.1).

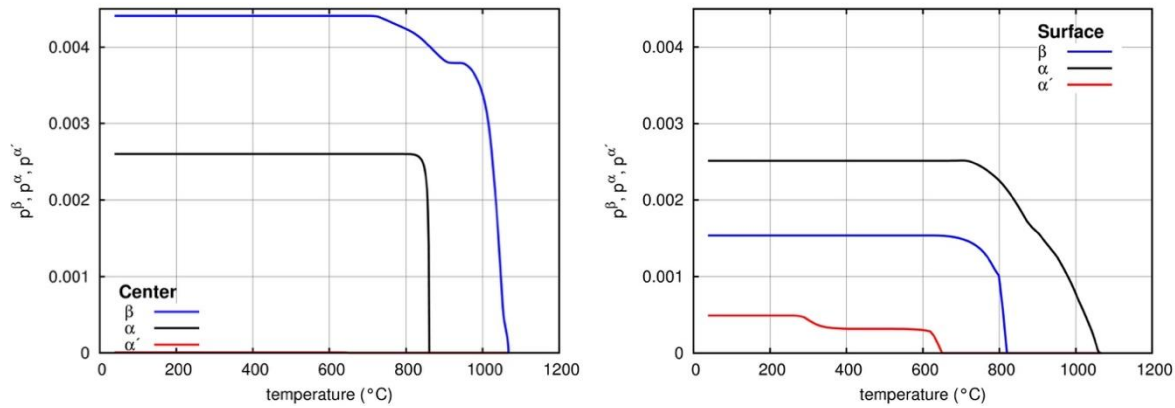

Figure 18. Cumulated equivalent plastic strain as a function of temperature in β, α and α' phases; a) center; b) surface of the cylinder.

The radial profiles of residual stresses predicted by the simulation are plotted in Figure 9b, along with the experiment. The average of the stresses calculated in α and α' phases are plotted, so that it can be compared to the results from neutron diffraction. The predicted residual stress profiles are characteristic of thermally induced stresses. The residual stresses come only from the plastic strains cumulated in α and β phases. Several trends are in accordance with the experiment: Tensile and compressive stresses are predicted respectively in the center and at the surface for the axial and tangential components. The simulated radial component has a lower magnitude than the experimental one in the center.
Despite the prediction of these trends, there are significant discrepancies regarding the magnitude of the residual stresses. For example, the axial residual stress in the center is underestimated by the simulation (350 MPa according to the simulation and 590 MPa according the experiment). Discrepancies can be seen also for the axial and hoop stress in the radius area 14-16mm (underestimation by the simulation). Accordingly, the elastic strains are underestimated, as shown in Figure 9a (average elastic strain in α and α' phases is plotted). The origin of these discrepancies will be discussed in Section 5.

5 Discussion

The following discussion will focus mainly on the influence of phase transformations on the formation of residual stresses and the discrepancies between calculated and measured residual stresses.

5.1 The case without phase transformation: quenching of Ti17

Experimental residual stress profiles are representative of the thermally induced residual stresses in the Ti17 alloy cylinder. This was expected, as no phase transformation occurred because of the β-metastable character of the Ti17 alloy and the small size of the sample. The results of the simulations in the Ti17 alloy mainly depend on the prediction of the temperatures fields during quenching and on the mechanical behavior of the β phase. The latter was established experimentally between 920°C and 700°C but between 700°C and room temperature, it had to be extrapolated. This concerns mainly the regions near the surface, which plastically deform significantly down to low temperatures (between 700°C and 400°C see Figure 15), while near the center, the stresses become quickly too low to induce plastic deformation.
The situation would have been different if a more massive part had been quenched. The inner regions would have transformed and would have undergone higher stresses. The regions near the surface would have remained in the β phase. The material mechanical behavior would thus have been required to be established over a large temperature range, not only in the β, but also in the α+β field.

5.2 The effect of phase transformations: quenching of Ti-6Al-4V

5.2.1 From the changes in thermomechanical and thermal behaviors

The most natural effect of the phase transformations is to modify the thermomechanical behavior of the material as well as its thermophysical properties together with the microstructure. The latent heat released by the β→α+β/α' phase transformations also induces complex temperature evolutions inside the Ti-6Al-4V cylinder during the cooling.

Nevertheless, as described in Section 4.2.2, the internal stresses evolutions are only weakly and temporarily disrupted by the phase transformations during the quench, according to the simulation (Figure 17). In order to further analyze these effects, other simulations are shown here with different assumptions regarding the phase transformations:

- Suppression of the latent heat.
- Imposing extremely fast $\beta \rightarrow \alpha+\beta$ phase transformation kinetics: the α phase volume fraction follows the z_{max} parameter as a function of temperature (equation 7).
- Suppressing the phase transformation: the alloy remains in β state.

Results of these simulations are presented in Figure 19, focusing on the radial profile of axial residual stresses. Overall outcome is that the magnitude of the residual stresses is not strongly different whatever the considered assumption. Suppressing the phase transformation heat release induces negligible changes in the predicted residual stresses. Assuming extremely fast phase transformation kinetics modifies weakly the calculated residual stress. This suggests at first sight that an accurate prediction of the phase transformation kinetics is not necessary. More surprisingly, full suppression of the phase transformation does not modify significantly the predictions (about 40 MPa variation).

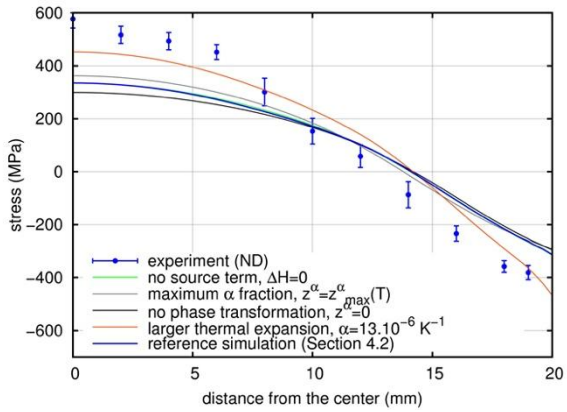

Figure 19 Radial profile of axial residual stress in the median plane according to the experiment (neutron diffraction) and to the simulation with three assumptions regarding the phase transformations: with the metallurgical model presented in Section 3.2 (same simulation as in Section 4.2); without latent heat source term; with higher thermal expansion coefficient 13.10^{-6} K^{-1}; extremely fast phase transformation kinetics (fraction of α phase follows $z^{\alpha}_{max}(T)$, equation 7); without phase transformation (the alloy remains in the β state).

The origin of these weak effects of phase transformations is two-fold. First, the unique origin of the residual stresses in these simulations is the plastic strains which are accumulated in the material during the cooling. Second, a large part of these plastic strains is accumulated before the phase transformations have started, while the alloy is still in a full β state. This is illustrated in Figure 18: both at the center and the surface, the equivalent cumulated plastic strain is higher in the β phase and it is accumulated in most part before the start of the $\beta \rightarrow \alpha+\beta$ phase transformation. Then, the α phase cumulates a lower amount of plastic strain, because the material is stronger at lower temperature. Moreover, the α phase itself strengthens quickly the material. Several comments can be done from these results:

- Accurate knowledge of the thermomechanical behavior of the β phase is necessary for a precise prediction of the internal stresses, as most plastic strains are cumulated in the full β state.
- From the preceding, the prediction of phase transformation kinetics may seem useless at first sight. Nevertheless, this knowledge is necessary, because the start of the phase transformations determines at which temperature the plastic deformations will slow down

and rapidly stop. This is illustrated by the case of the Ti17 alloy, without phase transformation: at the surface, plastic straining goes on down to ca. 400°C (Figure 15). In Ti-6Al-4V alloy, this minimum temperature is higher, about 750°C (Figure 18), because of the phase transformation which increases the yield strength.

- Accurate knowledge of the mechanical behavior in the presence of α phase and at low temperature is not necessary in present study, as few plastic straining occurs once the phase transformation has started. Indeed, the phase transformation kinetics is fast and the α phase strengthens quickly the material. Detailed accounting of the α phase morphology is therefore even less relevant in this case.
- This last conclusion would not apply though on titanium alloys which are less α-stabilized, with slower phase transformations kinetics and lower amount of α phase at equilibrium, letting plastic deformations occur in a larger temperature range and inside an α+β microstructure with significant volume fraction of both α and β phases. Considering more massive parts would also involve more plastic straining in the α+β state.

5.2.2 From the strains induced by the phase transformation

According to the experiments, the phase transformations which occurred during the quench of the Ti-6Al-4V alloy cylinder did not influence significantly the residual stresses. Indeed, the radial profiles of residual stresses are characteristic of thermally-induced stresses (compressive at the surface, tensile in the center). The presence of a microstructural gradient (more α' phase and higher hardness near the surface, see Figure 4) has no visible influence on the distribution of residual stresses. Accordingly, the simulations predict that the internal stress evolutions are weakly and temporarily disturbed during the quench (Figure 17). Finally, the effects of the phase transformations on the material behavior have a weak impact, as seen in a previous section.

More visible effects would have occurred if the transformation strains associated with the β→α+β/α' phase transformations (volume change, phase transformation plasticity) had been more significant. The volume change induced by phase transformations is small or negligible in titanium alloys (e.g. [22]). Accordingly, our cooling experiments in a dilatometer did not allow to detect any volume change due to the phase transformation. As for the phase transformation plasticity, it was put into evidence in previous studies on Ti-6Al-4V alloy [68,69], but considering a lower applied stress and slower temperature evolutions than during our quench experiment. For these reasons, the simulations presented in Section 4.2 were carried out by assuming that the volume change and the transformation plasticity strains are equal to zero. This assumption is corroborated by the satisfactory comparison between simulation and experiment, regardless of the magnitude of the residual stresses.

In order to fully ascertain whether or not the effects of phase transformation strains should be considered, additional simulations are carried out here by assuming now the presence of a strain due to volume variation and of a transformation plasticity strain. The volume expansion $\Delta V/V_0$ associated with both β→α and β→α'transformations is assumed to be equal to 0.2% ($\delta=6.7.10^{-4}$ in equation 13). This is the maximum value reported in literature.

Figure 20 shows the calculated radial profile of the axial residual stress from three simulations: without phase transformation induced strains (the simulation presented in Section 4.2), with volume change strain alone and with both volume change and transformation plasticity strains. The first outcome is that the accounting of the phase change strains did not modify significantly the residual stress distributions, which remain typical of thermal-induced stresses. The magnitude of the stresses remains far from the experiment, especially in the

center. With the accounting of the sole volume change strain, the magnitude of the predicted residual stresses becomes even lower than in the reference case. It can be explained for example at the surface where the internal stresses are tensile when the phase transformation occurs (see Figure 17): the positive phase transformation volume change will reduce the internal stress level. Therefore, less plastic strains are cumulated than in the reference case.
Conversely, adding the transformation plasticity strain in the simulation increased the magnitude of the residual stresses, compared to the reference case. When the phase transformation occurs, significant transformation plasticity strain is cumulated. The cumulated equivalent plasticity strain (ε^{tp}) reaches for instance 0.47% and 0.25% respectively at the center and the surface. This additional source of "plastic" strain increases the residual stresses, which remain however far from the experiment. These simulations confirm that the strains induced by the β→α+β/α' phase transformations have limited consequences on the formation of the internal stresses. One nevertheless points out that a rough estimate has been done for the transformation plasticity strain. Indeed, transformation plasticity may also result from orientation effects, particularly for the martensitic transformation. Further experimental characterization should be carried out to quantify this origin of transformation plasticity.

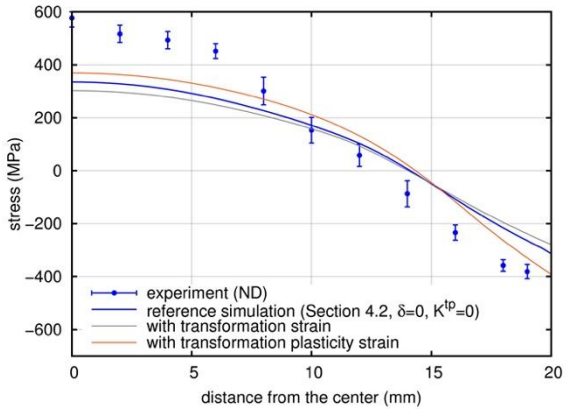

Figure 20. Radial profile of axial residual stress in the median plane according to the experiment (neutron diffraction) and to the simulation with three assumptions: phase change strains equal to zero; accounting of a volume change strain; accounting of both volume change and transformation plasticity strains.

5.3 Discrepancies between simulation and experiment for Ti-6Al-4V

The simulation underestimates the magnitude of the residual stresses in the Ti-6Al-4V alloy, as compared with both neutron diffraction and hole drilling experimental methods in the surface area as well as in the center (Figure 9). Apart from the discrepancies regarding thermal simulations, several possible origins can be given for the material model, with increasing impact:

- The lack of accuracy of the thermomechanical model in α+β state: its parameters were identified (Section 3.3.3.5) from tensile test experiments [19] which were done on samples having a coarse α+β microstructure, (with presence of primary α morphology). In the present study, the α phase morphology is finer, as a result of the fast cooling from the β range (Figure 5). Therefore, the simulations presented above underestimated the alloy strength in presence of the α phase. Nevertheless, this implies that the plastic strains, and thus the residual stresses, have been overestimated. Moreover, the weak impact of the thermomechanical model in α+β state has been pointed out in Section 5.2.1: once the α

phase has started to form, the alloy strengthens quickly, which stops rapidly the plastic deformations, whatever the detailed thermomechanical behavior of the $\alpha+\beta$ mixture.

- Kinematic hardening was not considered, whereas the different parts of the cylinder undergo successively stresses of opposite sign. (For example, tensile stress followed by compressive stress at the surface).
- A more important source of inaccuracy is the lack of knowledge regarding the thermomechanical behavior of the β phase for the Ti-6Al-4V alloy. Most available data were established in the context of industrial hot processing (e.g. [63,64,70,71]), i.e. considering much larger strains and strain rates than those generated during quenching operations (strain~1%, strain rate ca. 10^{-4}-10^{-3} s^{-1}). When the Ti-6Al-4V alloy is characterized under these conditions of strain and strain rate, it is done at temperatures where there is a majority of α phase in the microstructure (e.g. [19,65]). One can stress that the predictions are more accurate for the Ti17 alloy (which remained in a full β state). This comes from the more accurate knowledge of the mechanical behavior in a full β state, which was established experimentally in detail in [62] for this alloy, and which served to identify the model parameters in [16].
- Transformation plasticity strain should be considered, as mentioned in a previous Section.

Finally, a great uncertainty concerns the thermal expansion coefficient of the β and α phases. This is a key parameter for the simulations, as the internal stresses are induced by the temperature gradients which develop inside the cylinder during the quench. We carried out dilatometry experiments on three different samples in order to establish the thermal expansion coefficients. For each experiment, significantly different values were identified, spanning a range 9.0-13.1 10^{-6} K^{-1} for the α phase and a range 11.5-12.8 10^{-6} K^{-1} for the β phase. Moreover, the direction of cutting of the dilatometry sample from the billet, longitudinally or transversally, seems to play a role, although no trend could be established. This suggests possible effects of crystallographic texture. Accordingly, significant spread of thermal expansion coefficient values is reported in literature [14,22,72,73]. Only one study [72] gives a value for the β phase. This is an important parameter, as most of the plastic strains are cumulated while the alloy is still in a full β state (Section 5.2.1).
In order to show the impact of the thermal expansion coefficient on the simulations, the same simulation as presented in Section 4.2 is done here by assuming a thermal expansion coefficient of 13.10^{-6} K^{-1} for both α and β phases, instead of 10^{-5} K^{-1} previously: see Figure 19. Closer agreement with the experiment is obtained, thus showing that this parameter can be one of the causes of the underestimation of the residual stresses. For instance, the axial stress in the center was 460 MPa instead of 350 MPa (experiment is 580 MPa). The agreement regarding the elastic strains, not shown here, is even more convincing.

6 Conclusion

The formation of macroscopic internal stresses occurring during the water quenching of Ti17 and Ti-6Al-4V alloy laboratory samples has been investigated experimentally as well as by simulation, in order to establish any possible influence of phase transformations. Two cylindrical samples with the same geometry (diameter 40 mm) were water quenched after a solution treatment in the β phase field. The samples were instrumented with thermocouples to track the temperature evolutions in the median plane. The microstructure was characterized after the quench. Residual stresses were determined by neutron diffraction in the bulk of the samples, by the hole drilling method near the surface and by the contour method over both the bulk and the surface of the samples.

The β-metastable Ti17 alloy sample did not undergo any phase transformation: it remained in a full β state because of the fast cooling. Residual stresses were typical of thermally-induced stresses evolutions: compressive at the surface and tensile in the center. The simulation confirms that the internal stress evolutions are governed by the temperature gradients established in the cylinder during the cooling. Satisfactory prediction of the residual stresses is possible thanks to a thermomechanical model established previously. An important basis of this model is the accurate knowledge of the thermomechanical behavior of the alloy in the β state, and over a large range of temperatures, from 920°C down to 700°C.
The α+β Ti-6Al-4V alloy underwent β→α+β and β→α' phase transformations during the quench. A gradient of microstructure and hardness was established, with higher hardness and a higher amount of martensite near the surface because of the faster cooling. Despite the microstructural evolutions and the gradient of microstructures, the distribution of residual stresses remained typical of thermally-induced internal stress evolutions, like for the Ti17 alloy sample. Hence, the phase transformations have a weak impact on the internal stress evolutions and the residual stresses, according to the experiment.
A coupled thermal, metallurgical (phase transformation kinetics) and mechanical model was established in order to simulate the quenching. The simulation confirms that the phase transformations have a weak "direct" impact on the internal stress evolutions, both via the modification of thermal/mechanical behavior and via the volume change and transformation plasticity strains that they induce. Nevertheless, phase transformation kinetics predictions cannot be neglected in the simulations. One has to predict when the phase transformation will start, because the phase transformation quickly strengthens the material and this puts an end to the accumulation of the plastic strains at the origin of the residual stresses. The plastic strains are cumulated in most part when the Ti-6Al-4V is still in a full β state. Therefore, an accurate knowledge of the thermomechanical behavior of β phase should be established from experimentation for more accurate predictions in this alloy. Although this study focused on quenching, these conclusions are expected to remain relevant in the framework of processing by e.g. welding or additive manufacturing. Future work should address the effect of crystallographic texture on the thermal expansion coefficients and the consequences on the formation of thermal-induced stresses.

7 Acknowledgements

TIMET Savoie is gratefully acknowledged for providing both the Ti17 and the Ti-6Al-4V alloy materials, and for discussions with Yvon Millet. We wish to thank HZB for the allocation of neutron radiation beam time. The society Mat-in-Meca© is thanked for the residual stress determinations by the contour method. Special thanks for Patrice Poirot at IJL's Workshop for the design and machining operations to achieve the instrumentations with thermocouples.

8 Bibliography

[1] H.-W. Zoch, Distortion engineering: vision or ready to application?, in: H.-W. Zoch, T. Lübben (Eds.), Proc. 2nd Int. Conf. Distortion Eng. 2008, Bremen, Germany, 2008: pp. 3–12.
[2] R. Fechte-Heinen, T. Lübben, Quenching and distortion, in: Proc. ECHT 2021 QDE – 2nd Int. Conf. Quenching Distortion Eng., Online, 2021: pp. 189–208.
[3] S. Denis, P. Archambault, E. Gautier, A. Simon, G. Beck, Prediction of residual stress

and distortion of ferrous and non-ferrous metals: Current status and future developments, J. Mater. Eng. Perform. 11 (2002) 92–102. https://doi.org/10.1007/s11665-002-0014-2.
[4] S. Denis, S. Sjöström, A. Simon, Coupled temperature, stress, phase transformation calculation, Metall. Trans. A. 18 (1987) 1203–1212. https://doi.org/10.1007/BF02647190.
[5] S. Denis, J.C. Chevrier, G. Beck, Étude des contraintes résiduelles introduites par la trempe dans des cylindres en TA6ZrD (685), J. Common Met. 69 (1980) 265–276. https://doi.org/10.1016/0022-5088(80)90059-4.
[6] S. Denis, D. Farias, A. Simon, Mathematical Model Coupling Phase Transformations and Temperature Evolutions in Steels, ISIJ Int. 32 (1992) 316–325. https://doi.org/10.2355/isijinternational.32.316.
[7] S. Denis, E. Gautier, S. Sjöström, A. Simon, Influence of stresses on the kinetics of pearlitic transformation during continuous cooling, Acta Metall. 35 (1987) 1621–1632. https://doi.org/10.1016/0001-6160(87)90109-X.
[8] E. Gautier, A. Simon, G. Beck, Plasticite de transformation durant la transformation perlitique d'un acier eutectoïde, Acta Metall. 35 (1987) 1367–1375. https://doi.org/10.1016/0001-6160(87)90019-8.
[9] S. Denis, P. Archambault, E. Gautier, SECTION 9.12 - Models for Stress-Phase Transformation Couplings in Metallic Alloys, in: J. Lemaitre (Ed.), Handb. Mater. Behav. Models, Academic Press, Burlington, 2001: pp. 896–904. https://doi.org/10.1016/B978-012443341-0/50091-0.
[10] D. Godard, P. Archambault, S. Denis, E. Gautier, F. Heymes, Modelling of heat treatment residual stresses. Application to high strength aluminum alloys including precipitation effects, in: Proc. 7th Int. Semin. Heat Treat. End Surf. Eng. Light Alloys, Hungarian Scientific Society of Mechanical Engineering, Budapest, Hungary, 1999: pp. 249–258.
[11] N. Chobaut, D. Carron, P. Saelzle, J.-M. Drezet, Measurements and Modeling of Stress in Precipitation-Hardened Aluminum Alloy AA2618 during Gleeble Interrupted Quenching and Constrained Cooling, Metall. Mater. Trans. A. 47 (2016) 5641–5649. https://doi.org/10.1007/s11661-016-3724-z.
[12] R. Turner, R.M. Ward, R. March, R.C. Reed, The Magnitude and Origin of Residual Stress in Ti-6Al-4V Linear Friction Welds: An Investigation by Validated Numerical Modeling, Metall. Mater. Trans. B. 43 (2012) 186–197. https://doi.org/10.1007/s11663-011-9563-9.
[13] W. Rae, Thermo-metallo-mechanical modelling of heat treatment induced residual stress in Ti–6Al–4V alloy, Mater. Sci. Technol. 35 (2019) 747–766. https://doi.org/10.1080/02670836.2019.1591031.
[14] Y. Robert, Simulation of YAG pulse laser welding of titanium alloy (TA6V), PhD thesis, École Nationale Supérieure des Mines de Paris, 2007. https://pastel.archives-ouvertes.fr/pastel-00003117.
[15] A. Longuet, Y. Robert, E. Aeby-Gautier, B. Appolaire, J.F. Mariage, C. Colin, G. Cailletaud, A multiphase mechanical model for Ti–6Al–4V: Application to the modeling of laser assisted processing, Comput. Mater. Sci. 46 (2009) 761–766. https://doi.org/10.1016/j.commatsci.2009.05.012.
[16] J. Teixeira, B. Denand, E. Aeby-Gautier, S. Denis, Simulation of coupled temperature, microstructure and internal stresses evolutions during quenching of a β -metastable titanium alloy, Mater. Sci. Eng. A. 651 (2016) 615–625. https://doi.org/10.1016/j.msea.2015.11.010.
[17] J. Ahn, E. He, L. Chen, R.C. Wimpory, J.P. Dear, C.M. Davies, Prediction and measurement of residual stresses and distortions in fibre laser welded Ti-6Al-4V considering phase transformation, Mater. Des. 115 (2017) 441–457. https://doi.org/10.1016/j.matdes.2016.11.078.

[18] P. Tan, F. Shen, B. Li, K. Zhou, A thermo-metallurgical-mechanical model for selective laser melting of Ti6Al4V, Mater. Des. 168 (2019) 107642. https://doi.org/10.1016/j.matdes.2019.107642.
[19] R. Julien, Thermomechanical behaviour and microstructural evolution of a forged α+β – Ti-6Al-4V alloy during quenching : experiments, analysis and modelling, PhD thesis, Ecole des Mines d'Albi-Carmaux, 2017. https://tel.archives-ouvertes.fr/tel-01560068.
[20] R. Julien, Tensile behaviour of high temperature forged Ti-6Al-4V during in-situ heat treatments, Mater. Lett. 208 (2017) 7. https://doi.org/10.1016/j.matlet.2017.05.050.
[21] R. Julien, V. Velay, V. Vidal, Y. Dahan, R. Forestier, F. Rézaï-Aria, Characterization and modeling of forged Ti-6Al-4V Titanium alloy with microstructural considerations during quenching process, Int. J. Mech. Sci. 142–143 (2018) 456–467. https://doi.org/10.1016/j.ijmecsci.2018.05.023.
[22] A.K. Swarnakar, O. Van der Biest, B. Baufeld, Thermal expansion and lattice parameters of shaped metal deposited Ti–6Al–4V, J. Alloys Compd. 509 (2011) 2723–2728. https://doi.org/10.1016/j.jallcom.2010.12.014.
[23] W. Rae, Z. Lomas, M. Jackson, S. Rahimi, Measurements of residual stress and microstructural evolution in electron beam welded Ti-6Al-4V using multiple techniques, Mater. Charact. 132 (2017) 10–19. https://doi.org/10.1016/j.matchar.2017.07.042.
[24] J.D.C. Teixeira, B. Appolaire, E. Aeby-Gautier, S. Denis, G. Cailletaud, N. Späth, Transformation kinetics and microstructures of Ti17 titanium alloy during continuous cooling, Mater. Sci. Eng. A. 448 (2007) 135–145. https://doi.org/10.1016/j.msea.2006.10.024.
[25] G. Flament, F. Moreaux, G. Beck, Instabilite de la calefaction a haute temperature sur un cylindre vertical trempe dans un liquide sous-refroidi, Int. J. Heat Mass Transf. 22 (1979) 1059–1067. https://doi.org/10.1016/0017-9310(79)90179-0.
[26] R. Dąbrowski, The Kinetics of Phase Transformations During Continuous Cooling of the Ti6Al4V Alloy from the Single-Phase β Range, Arch. Metall. Mater. 56 (2011) 703–707. https://doi.org/10.2478/v10172-011-0077-x.
[27] Y. Combres, Traitements thermiques des alliages de titane, Tech. Ing. (2013). https://www.techniques-ingenieur.fr/base-documentaire/materiaux-th11/traitements-thermiques-des-aciers-des-alliages-et-des-fontes-42364210/traitements-thermiques-des-alliages-de-titane-m1335/.
[28] S. Malinov, P. Markovsky, W. Sha, Z. Guo, Resistivity study and computer modelling of the isothermal transformation kinetics of Ti–6Al–4V and Ti–6Al–2Sn–4Zr–2Mo–0.08Si alloys, J. Alloys Compd. 314 (2001) 181–192. https://doi.org/10.1016/S0925-8388(00)01227-5.
[29] T. Ahmed, H.J. Rack, Phase transformations during cooling in alpha+beta titanium alloys, Mater. Sci. Eng. A. (1998) 6. https://doi.org/10.1016/S0921-5093(97)00802-2.
[30] C. Randau, U. Garbe, H.-G. Brokmeier, StressTextureCalculator: a software tool to extract texture, strain and microstructure information from area-detector measurements, J. Appl. Crystallogr. 44 (2011) 641–646. https://doi.org/10.1107/S0021889811012064.
[31] P.J. Withers, M.R. Daymond, M.W. Johnson, The precision of diffraction peak location, J. Appl. Crystallogr. 34 (2001) 737–743. https://doi.org/10.1107/S002188980101411X.
[32] P.J. Withers, M. Preuss, A. Steuwer, J.W.L. Pang, Methods for obtaining the strain-free lattice parameter when using diffraction to determine residual stress, J. Appl. Crystallogr. 40 (2007) 891–904. https://doi.org/10.1107/S0021889807030269.
[33] B. Eigenmann, E. Macherauch, Röntgenographische Untersuchung von Spannungszuständen in Werkstoffen. Teil III. Fortsetzung von Matwiss. und Werkstofftechn. Heft 3/1995, S. 148-160 und Heft 4/1995, S. 199-216, Mater. Werkst. 27 (1996) 426–437. https://doi.org/10.1002/mawe.19960270907.

[34] E28 Committee, Test Method for Determining Residual Stresses by the Hole-Drilling Strain-Gage Method, ASTM International, n.d. https://doi.org/10.1520/E0837-20.
[35] S. Fréour, D. Gloaguen, M. François, R. Guillén, Application of inverse models and XRD analysis to the determination of Ti-17 β-phase coefficients of thermal expansion, Scr. Mater. 54 (2006) 1475–1478. https://doi.org/10.1016/j.scriptamat.2005.12.051.
[36] E. Aeby-Gautier, B. Denand, J. Teixeira, M. Dehmas, B. Appolaire, A. Settefrati, Influence of microstructure on tensile properties of beta-metastable Ti17 alloy, in: Proc. 12th World Conf. Titan., The Nonferrous Metals Society of China, Beijing, China, 2011: pp. 1191–1195.
[37] M. Prime, A. Gonzales, The Contour Method: simple2-D mapping of residual stresses, in: Proceedings, Los Alamos National Lab. (LANL), Los Alamos, NM (United States), Oxford, UK, 2000: pp. 617–624. https://www.osti.gov/biblio/769066.
[38] M.B. Prime, A.T. DeWald, The Contour Method, in: Pract. Residual Stress Meas. Methods, John Wiley & Sons, Ltd, 2013: pp. 109–138. https://doi.org/10.1002/9781118402832.ch5.
[39] F. Hosseinzadeh, J. Kowal, P.J. Bouchard, Towards good practice guidelines for the contour method of residual stress measurement, J. Eng. 2014 (2014) 453–468. https://doi.org/10.1049/joe.2014.0134.
[40] F. Hosseinzadeh, P.J. Bouchard, Mapping Multiple Components of the Residual Stress Tensor in a Large P91 Steel Pipe Girth Weld Using a Single Contour Cut, Exp. Mech. 53 (2013) 171–181. https://doi.org/10.1007/s11340-012-9627-z.
[41] Y. Traore, S. Paddea, P.J. Bouchard, M.A. Gharghouri, Measurement of the Residual Stress Tensor in a Compact Tension Weld Specimen, Exp. Mech. 53 (2013) 605–618. https://doi.org/10.1007/s11340-012-9672-7.
[42] F. Hosseinzadeh, M. Burak Toparli, P. John Bouchard, Slitting and Contour Method Residual Stress Measurements in an Edge Welded Beam, J. Press. Vessel Technol. 134 (2011). https://doi.org/10.1115/1.4004626.
[43] M.B. Prime, Cross-Sectional Mapping of Residual Stresses by Measuring the Surface Contour After a Cut, J. Eng. Mater. Technol. 123 (2000) 162–168. https://doi.org/10.1115/1.1345526.
[44] M.B. Prime, Contour Method Advanced Applications: Hoop Stresses in Cylinders and Discontinuities, in: T. Proulx (Ed.), Eng. Appl. Residual Stress Vol. 8, Springer, New York, NY, 2011: pp. 13–28. https://doi.org/10.1007/978-1-4614-0225-1_2.
[45] C. Geuzaine, J.-F. Remacle, Gmsh: A 3-D finite element mesh generator with built-in pre- and post-processing facilities, Int. J. Numer. Methods Eng. 79 (2009) 1309–1331. https://doi.org/10.1002/nme.2579.
[46] Electricité de France, Analyse mécanique et thermo-mécanique pour des études et des recherches, 1989. www.code-aster.org.
[47] M.B. Prime, R.J. Sebring, J.M. Edwards, D.J. Hughes, P.J. Webster, Laser surface-contouring and spline data-smoothing for residual stress measurement, Exp. Mech. 44 (2004) 176–184. https://doi.org/10.1007/BF02428177.
[48] Y. Ohmori, K. Nakai, H. Ohtsubo, M. Tsunofuri, Formation of Widmanstätten Alpha Structure in a Ti–6Al–4V Alloy, Mater. Trans. JIM. 35 (1994) 238–246. https://doi.org/10.2320/matertrans1989.35.238.
[49] S. Malinov, W. Sha, Z. Guo, C.C. Tang, A.E. Long, Synchrotron X-ray diffraction study of the phase transformations in titanium alloys, Mater. Charact. 48 (2002) 279–295. https://doi.org/10.1016/S1044-5803(02)00286-3.
[50] B. Hocheid, R. Klima, C. Beauvais, M. Rapin, C. Roux, Contribution à l'étude des transformations de l'alliage TA6V en condiitons isothermes, Mém. Sci. Rev. Métallurgie. 67 (1970).

[51] M. Majdic, G. Ziegler, Effect of the metastable beta phase transformation in Ti-6Al-4V alloy, Z. Für Met. Mater Res Adv Tech. 64 (1973) 751–758.
[52] S.M. Kelly, Thermal and Microstructure Modeling of Metal Deposition Processes with Application to Ti-6Al-4V, 2004. https://vtechworks.lib.vt.edu/handle/10919/29731.
[53] R. Castro, L. Séraphin, Contribution in the metallographic and structural study of the alloy of titanium TA6V, Mém. Sci. Rev. Métallurgie. 63 (1966) 1025–1028.
[54] A. Crespo, A. Deus, R. Vilar, Modeling of phase transformations and internal stresses in laser powder deposition, in: XVII Int. Symp. Gas Flow Chem. Lasers High-Power Lasers, International Society for Optics and Photonics, 2009: p. 713120. https://doi.org/10.1117/12.817405.
[55] C.C. Murgau, R. Pederson, L.E. Lindgren, A model for Ti–6Al–4V microstructure evolution for arbitrary temperature changes, Model. Simul. Mater. Sci. Eng. 20 (2012) 055006. https://doi.org/10.1088/0965-0393/20/5/055006.
[56] G. Cailletaud, Une approche micromécanique du comportement des polycristaux, Rev. Phys. Appliquée. 23 (1988) 353–365. https://doi.org/10.1051/rphysap:01988002304035300.
[57] G. Cailletaud, P. Pilvin, Utilisation de modèles polycristallins pour le calcul par éléments finis, Rev. Eur. Éléments Finis. 3 (1994) 515–541. https://doi.org/10.1080/12506559.1994.10511147.
[58] X. Wang, H. Hamasaki, M. Yamamura, R. Yamauchi, T. Maeda, Y. Shirai, F. Yoshida, Yield-Point Phenomena of Ti-20V-4Al-1Sn at 1073 K and Its Constitutive Modelling, Mater. Trans. 50 (2009) 1576–1578. https://doi.org/10.2320/matertrans.M2009059.
[59] J. Da Costa Teixeira, Experimental study and modeling of the microstructure evolutions during the cooling after forging in the titanium alloy Ti17, Theses, Institut National Polytechnique de Lorraine, 2005. https://tel.archives-ouvertes.fr/tel-01749978.
[60] F. Bruneseaux, E. Aeby-Gautier, G. Geandier, J. Da Costa Teixeira, B. Appolaire, P. Weisbecker, A. Mauro, In situ characterizations of phase transformations kinetics in the Ti17 titanium alloy by electrical resistivity and high temperature synchrotron X-ray diffraction, Mater. Sci. Eng. A. 476 (2008) 60–68. https://doi.org/10.1016/j.msea.2007.04.072.
[61] G.W. Greenwood, R.H. Johnson, The Deformation of Metals Under Small Stresses During Phase Transformations, Proc R Soc Lond A. 283 (1965) 403–422. https://doi.org/10.1098/rspa.1965.0029.
[62] M. Khelifa, E. Aeby-Gautier, S. Denis, P. Archambault, J.-P. Sarteaux, Analysis of the mechanical behavior of metastable titanium alloys – Influence of the phase transformation, in: Proc. 10th World Conf. Titan., Wiley-VCH, Hamburg, Germany, 2003: pp. 1599–1606.
[63] S. Bruschi, S. Poggio, F. Quadrini, M.E. Tata, Workability of Ti–6Al–4V alloy at high temperatures and strain rates, Mater. Lett. 58 (2004) 3622–3629. https://doi.org/10.1016/j.matlet.2004.06.058.
[64] J. Malcor, F. Montheillet, Behavior of titanium alloy Ti-6-percent Al-4-percent V in the range of hot heating, Mém. Etudes Sci. Rev. Métallurgie. 80 (1983) 89–103.
[65] M. Surand, Étude du comportement viscoplastique en traction et en fluage de l'alliage TA6V de 20 à 600 degrés Celsius, PhD Thesis, Université de Toulouse, 2013. http://ethesis.inp-toulouse.fr/archive/00002685/.
[66] J. Besson, R. Leriche, R. Foerch, G. Cailletaud, Object-Oriented Programming Applied to the Finite Element Method Part II. Application to Material Behaviors, Rev. Eur. Éléments Finis. 7 (1998) 567–588. https://doi.org/10.1080/12506559.1998.10511322.
[67] E. Macherauch, O. Vöhringer, Residual Stresses After Quenching, in: B. Liščić, H.M. Tensi, W. Luty (Eds.), Theory Technol. Quenching Handb., Springer, Berlin, Heidelberg, 1992: pp. 117–181. https://doi.org/10.1007/978-3-662-01596-4_6.
[68] D. Leriche, E. Gautier, A. Simon, Mechanical behaviour of a forged and HIP'ed

TA6V4 alloy in the phase transformation alpha+beta / beta temperature range, in: Proc. 6th World Conf. Titan., SF2M, Cannes, France, 1988: pp. 163–168.
[69] C. Schuh, D.C. Dunand, Non-isothermal transformation-mismatch plasticity: modeling and experiments on Ti–6Al–4V, Acta Mater. 49 (2001) 199–210. https://doi.org/10.1016/S1359-6454(00)00318-9.
[70] S.L. Semiatin, V. Seetharaman, I. Weiss, Flow behavior and globularization kinetics during hot working of Ti–6Al–4V with a colony alpha microstructure, Mater. Sci. Eng. A. (1999) 15. https://doi.org/10.1016/S0921-5093(98)01156-3.
[71] A. Majorell, S. Srivatsa, R.C. Picu, Mechanical behavior of Ti–6Al–4V at high and moderate temperatures —Part I: Experimental results, Mater. Sci. Eng. A. (2002) 9. https://doi.org/10.1016/S0921-5093(01)01507-6.
[72] J.W. Elmer, T.A. Palmer, S.S. Babu, E.D. Specht, In situ observations of lattice expansion and transformation rates of α and β phases in Ti–6Al–4V, Mater. Sci. Eng. A. 391 (2005) 104–113. https://doi.org/10.1016/j.msea.2004.08.084.
[73] H. Choo, P. Rangaswamy, M.A.M. Bourke, J.M. Larsen, Thermal expansion anisotropy in a Ti–6Al–4V/SiC composite, Mater. Sci. Eng. A. 325 (2002) 236–241. https://doi.org/10.1016/S0921-5093(01)01463-0.